

Article | Received 21 October 2025; Accepted 11 January 2025; Published date
<https://doi.org/10.55092/XXXX>

Pinned-surface and double-junction photodiode type super high-performance image sensor with built-in solar cell structure

Yoshiaki Daimon Hagiwara

President Office, Sojo University, Kumamoto-city, Japan

E-mail: hagiwara@ofc.sojo-u.ac.jp

Abstract: Floating surface single-junction type photodiodes are mostly used in solar cell applications for simplicity and cost. On the other hand, pinned-surface and double-junction type photodiodes are used now in super high-performance image sensor applications. This paper first reviews the difference between the conventional floating-surface single-junction type photodiode and the pinned-surface double-junction type photodiode. The pinned-surface buried-channel P+PNPP+ double junction type photodiodes are very high-performance image sensors with no image lag and very high light sensitivity compared to conventional ones. The diode can be applied not only to image sensors but also to solar cells. In addition, this paper proposes a new AI robot vision chip in the modern 3DIC CMOS image sensor technology using this double junction type diode. So, the diode will be widely interested in process, device, and application researchers and engineers for image sensors and solar cells. A real-time AI smart robot vision chip is described as an example of application, which is composed of an array of $N \times N$ pinned-surface buried-channel P+PNPP+ double junction type photo diodes, $N \times N$ analog-data stream mask-and-match comparators, digital processing and SRAM cache buffer memory units, integrated in a 3-D multichip architecture. In the external power-off mode, the image sensor array of $N \times N$ pinned-surface buried-channel P+PNPP+ double junction type photo diodes also function as a solar cell unit for the AI self-energy robot vision chip.

Keywords: pinned-surface; floating-surface; depletion width; image sensor; solar cell; energy efficiency; maximum power tracking technology; multi digital bit data comparator; 3DIC multichip

1. Introduction

Charge couple device (CCD) type charge transfer device (CTD), originally invented in 1970 [1], is composed of a series of MOS large-capacitor gates, and consumes a large power for charging and discharging the large CCD/MOS capacitors in order to perform the complete charge transfer operations. Thanks to the advancements in the long history [2–9] of modern low-power CMOS process scaling technology, CCD type CTD is now completely replaced by the low-power digital CMOS type CTD with the in-pixel source-follower current-amplifier circuit originally invented by Peter Noble in 1969 [10]. Since the size of the source-follower current amplifier circuit was too large to be included in each pixel,



Copyright©2025 by the authors. Published by ELSP. This work is licensed under Creative Commons Attribution 4.0 International License, which permits unrestricted use, distribution, and reproduction in any medium provided the original work is properly cited.

the buried-channel charge coupled device (CCD) type charge transfer device (CTD) [11] was used till late 1990s. Thanks to the modern CMOS scaled advanced process technology, in our high-definition digital TV era, MOS transistors and S/D contacts have now become small enough to be included in each pixel of image sensors. Charge Coupled Device (CCD) type was not the only charge transfer device (CTD) that transfers the information of one single photo electron for a long distance in a silicon chip. Image sensor in general is composed of three basic parts, (1) a light-sensing photodiode, (2) a signal charge transfer device (CTD) and (3) the image information processing unit as shown in Figure 1a.

Historically, the first original PNP double junction buried-channel type light-sensing photodiode was invented by Philips in Netherland on June 9, 1975 [12] as shown in Figure 1b. The dashed line in the figure shows the empty potential well in the buried channel for a single electron to move along for a long distance in the silicon chip. However, the surface P region was connected only to the high-resistivity substrate, with some undesired RC delay time to the substrate pinned ground voltage level. This device works only for low-frequency operations because of the RC delay time constant to the substrate.

At low frequency, the surface P-region can remain grounded and the buried N-region can be kept completely depleted of the majority carrier electrons. And with no minority carrier hole present for recombination in the buried N-channel region, this PNP double junction photodiode can transfer one single photo electron for a distance inside of the silicon chip without recombination at low frequency. For high frequency operations, however, the surface hole accumulation region must be pinned in order to function as a pinned virtual gate for realizing the no-image-lag feature with the high-frequency global and electronic shutter function capability, in order to realize high-performance video camera operations, completely free from any mechanical parts and any film media.

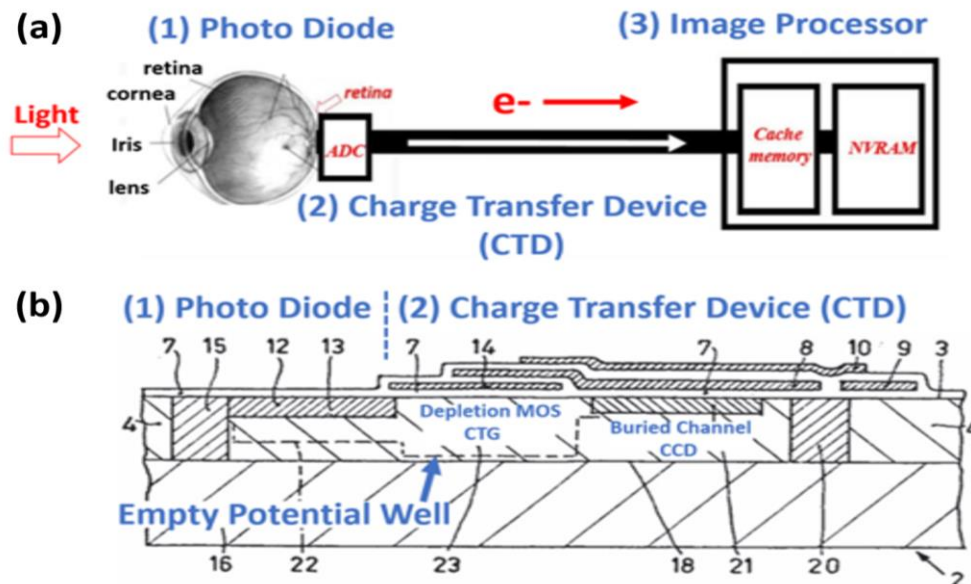


Figure 1. (a) an image sensor unit diagram and (b) a double-junction photodiode by Phillips [12].

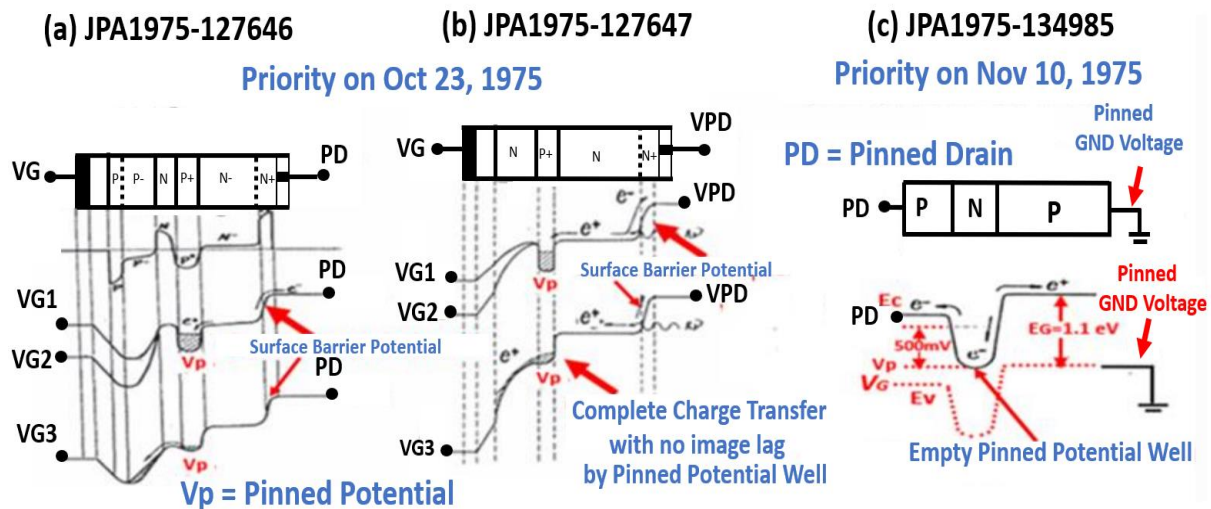


Figure 2. Pinned-surface and completely-depleted charge-collecting buried-storage photodiodes [13].

The unique double junction and triple junction devices were hinted by the Sony original double and triple junction type bipolar dynamic transistor technology [17]. High performance photodiodes invented by Sony in 1975 had a unique in-pixel vertical overflow drain (VOD) built-in structure with the global and electronic shutter capability, suitable for consumer video camera applications. See Figure 2. Sony filed in 1975 a series of these Japanese patent applications on the in-pixel pinned-surface and buried-channel double and triple junction photodiodes, but never disclosed the details until recently [14–16].

Sony photodiodes have the unique global and global shutter capability for capturing quick action pictures, free from any mechanical parts and replacing completely the film media by electronic media. A high-energy ion implantation technology with a unique lamp anneal method [18] was used to fabricate the pinned-surface P+PNPP+ double junction photodiode. Sony reported the complete charge transfer capability and the high quantum efficiency in the SSDM1977 and the SSDM1978 international conferences, and also in another domestic conference in Tokyo. Then, Sony was invited to talk at the CCD1979 conference in Edinburgh, Scotland UK and also at the ECS1980 conference in St. Louis, USA.

In 1979, Hyncek developed a virtual-phase CCD delay line with the complete charge transfer capability with the pinned-surface buried-channel PNP junction photodiode [19]. The pinned-surface of the PNP junction photodiode functions as a virtual gate for the complete charge transfer action. In 1982 NEC developed the buried-channel photodiode and used it in an ILT CCD type CTD image sensor with detailed measurement data of the image lag [20–21]. The NEC photodiode reported in IEDM1982 was identical with the Philips 1975 invention of the floating-surface PNP double junction buried photodiode. The surface hole accumulation was connected to the high resistivity substrate. In IEDM1984, Kodak emphasized the importance of the pinning the surface hole accumulation region to achieve the completely-no-image-lag feature. Kodak reported that there was no image lag and named the device as Pinned Photodiode [22], which is now widely known as the pinned-surface photodiode. The SSDM1978 conference paper by Sony and the IEDM1984 conference paper by KODAK both reported the excellent short-wave blue-light sensitivity with a very high quantum-efficiency of 60–80% on image sensor chips. However, no silicon chip is reported so far for solar cell applications. This paper explains the details.

The CCD type charge transfer device (CTD) is now completely replaced by the in-pixel source-follower current-amplifier circuit, originally invented in 1969 by Peter Noble, owing to the advancements of the scaled modern digital CMOS process technology.

However, the pinned-surface buried-channel P+PNPP+ double junction photodiode, invented in 1975 by Sony, has been used in the CCD video cameras in the analog TV era and also now widely in CMOS video cameras and smart phones in our modern digital TV era. This paper explains that a pinned-surface buried-channel double junction photodiode with a thin-film amorphous silicon base [23] has a good figure-of-merit in the cost-performance and the simplicity for solar cell applications and also for real-time AI smart robot vision 3DIC multichip applications.

2. Multi-chip 3DIC back-light illuminated CMOS image sensor for real-time AI robot vision

In this paper, a smart vision chip is explained in details, which is based on the original circuit architecture of a multi-bit digital-data comparator processor [24], a real-time high-performance digital engine, which was taught in the 1972 Caltech Digital Circuit Design Course, and was fabricated in the Intel 1972 Enhancement and Depletion (E/D) MOS process technology. See Figure 3. Under the guidance of Prof. C. A. Mead at Caltech, his EE graduate students designed the chip. It was a R/D project under the collaboration of a university and an industry for the first time in the world.

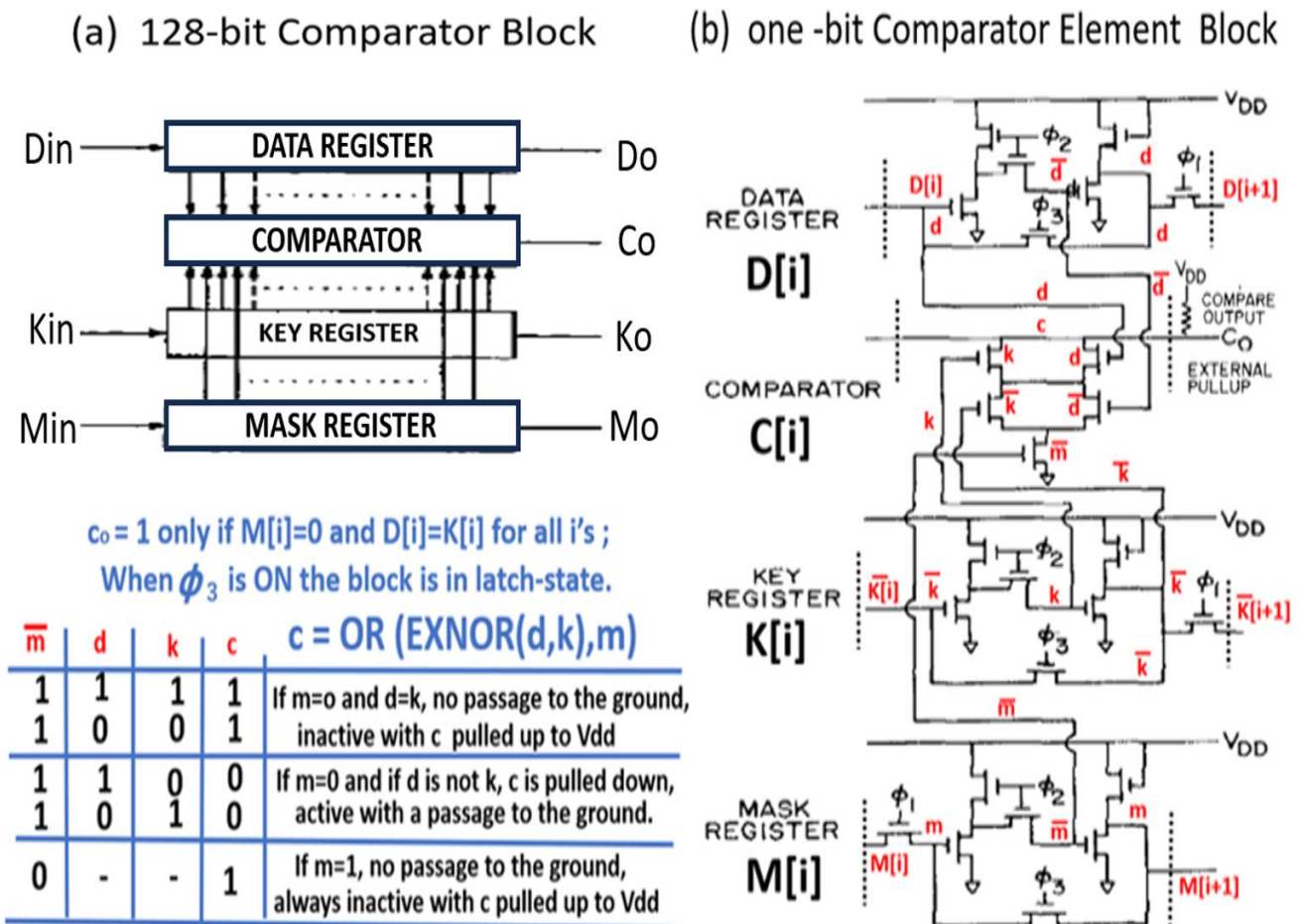


Figure 3. Full schematics of one bit slice of the 128-bit multi-comparator [24].

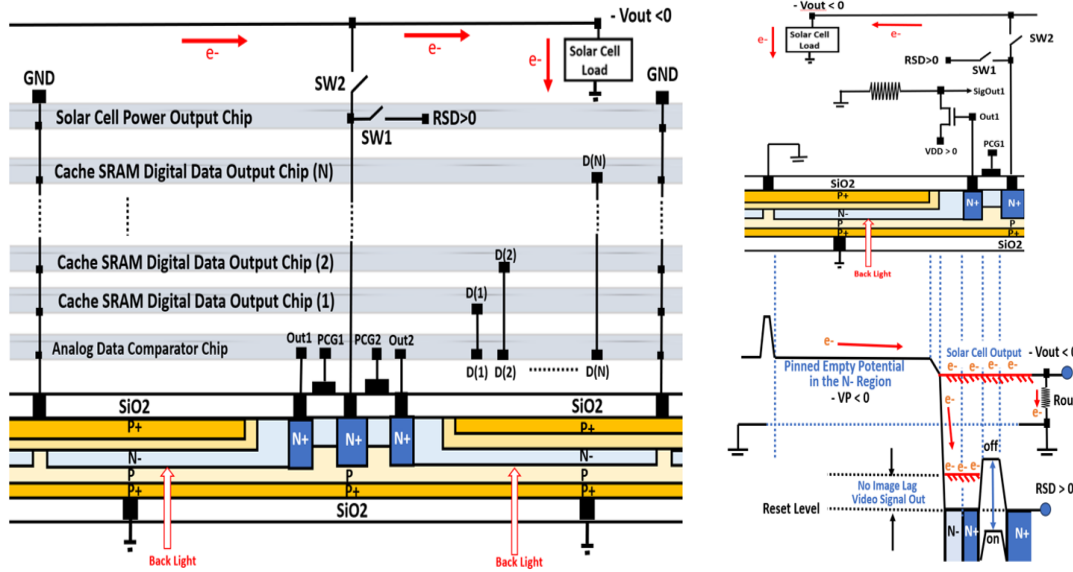


Figure 4. A cross-sectional view of our new AI Robot Vision chip in 3DIC multichip architecture.

Figure 4 shows a cross-sectional view of a smart robot vision chip in 3DIC multichip architecture [25–27]. A real-time AI smart robot vision chip is now proposed as an application in this paper, which is composed of the $N \times N$ analog-data steam mask-and-match comparators developed in 1972 by Caltech students as shown in Figure 3, an array of $N \times N$ pinned-surface buried-channel P+PNPP+ double junction type photo diodes invented in 1975 by Sony, and a high-speed cache SRAM buffer memory unit originally developed in 1989 by Sony [28]. All of them are integrated in a 3DIC multichip.

Figure 5 shows one-pixel unit of a unique high-performance image sensor unit, with the solar cell capability, which is composed of a pinned-surface buried-channel P+PNPP+ double junction photodiode with an in-pixel source-follower current-amplifier, and also with a depletion MOS type charge transfer gate (CTG) and another depletion MOS type pre-charging gate (PCG) with a switching outlet diffusion drain (ODD) region, for draining out the photo signal electrons. When in use for energizing the solar cell load, we have $\{SW1 = \text{off and } SW2 = \text{on}\}$. When not in use, we have $\{SW1 = \text{on and } SW2 = \text{off}\}$.

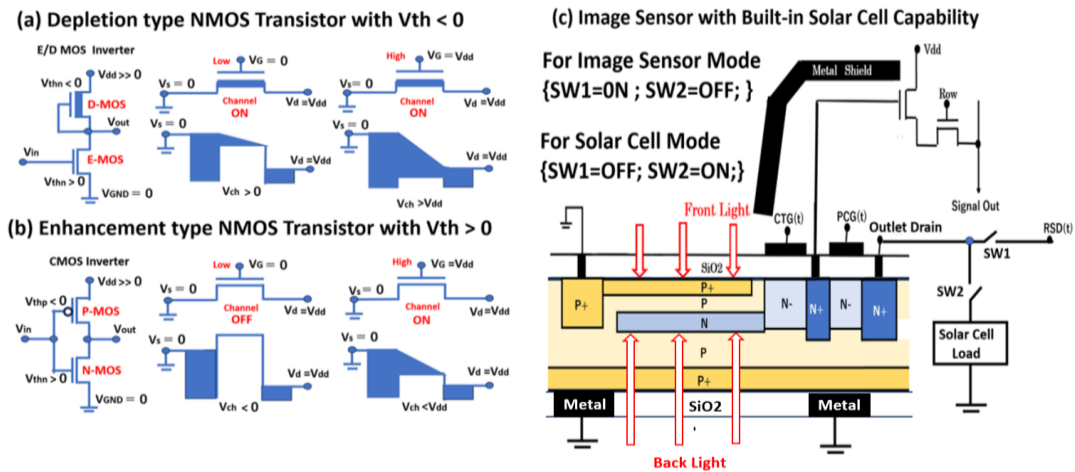


Figure 5. Active pixel image sensor with Depletion type CTG and PCG MOS Transistors.

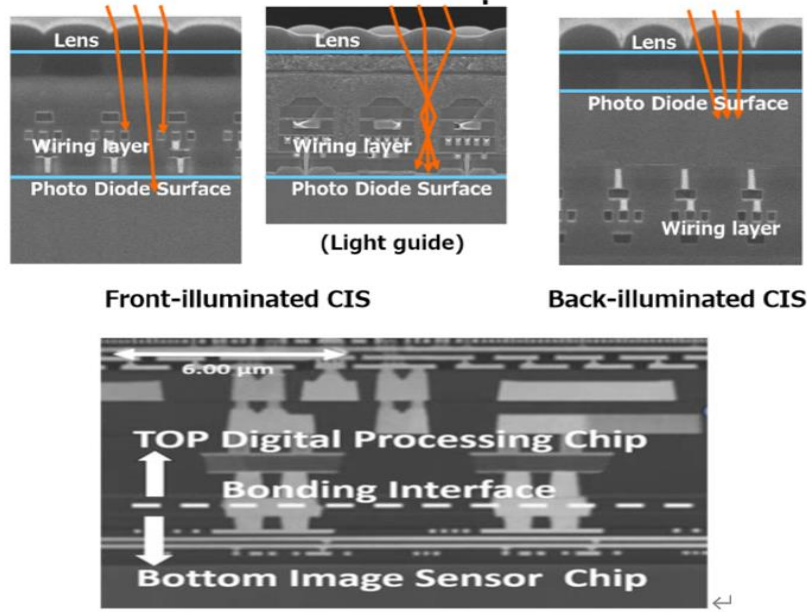


Figure 6. Cross sectional views of Sony 3D back-light CMOS image sensor [34].

Based on the early works [29–30], Sony now has the advanced CMOS scaled process and the 3DIC multi-chip complex packaging technology for realizing real-time smart robot vision chips. Figure 6 shows, by the courtesy of Sony corporation, the cross-sectional views in a 3DIC multichip architecture of a flash-image acquisition system developed by Sony [31–35].

3. Difference of floating-surface single junction and pinned-surface double junction photodiodes

Figure 7 shows a circuit model of (a) the floating-surfacer N+NPP+ single-junction-type solar cell and (b) the new pinned-surface P+PNPP+ double-junction-type solar cell.

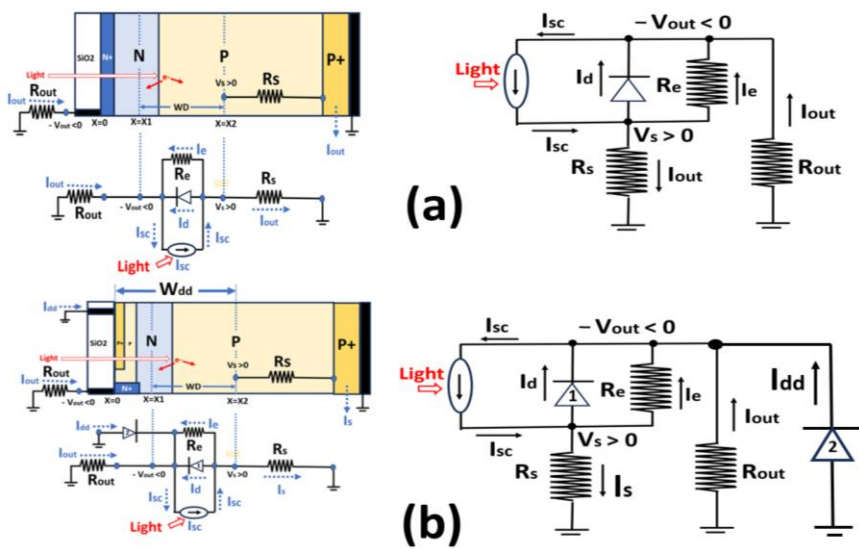


Figure 7. A circuit model of (a) the floating-surfacer N+NPP+ single-junction-type solar cell and (b) the proposed pinned-surface P+PNPP+ double-Junction solar cell in comparison.

In case of the floating-surface N+NPP+ single junction solar cell, the input solar cell current I_{sc} is given as (1) $\{I_{sc} = I_d + I_{out} + I_e;\}$ while the output voltage V_{out} is given as (2) $\{V_{out} = (I_{out})(R_{out});\}$ and the large P-type substrate resistance R_s is related with the output current I_{out} as (3) $\{V_s = (I_{out})(R_s);\}$. See Fig. 7(a). The small photo diode leakage current I_e is given as (4) $\{(V_s + V_{out}) = (I_e)(R_e);\}$ while the photo diode forward current I_d is given as (5) $\{I_d = I_o \exp ((V_{out} + V_s)/kT) - 1;\}$.

There are five equations (1) thru (5) with five unknown parameters $\{V_{out}, V_s, I_d, I_e, I_{out}\}$ which can be determined uniquely with the input independent parameters $\{I_{sc}, DP, DN, R_e, R_s, R_{out}\}$. By applying the maximum power tracking technology (MATT), the solar cell output power $= (I_{out})(V_{out})$ can be maximized by controlling the output solar cell voltage $\{V_{out} = (I_{out})(R_{out});\}$.

The values of DP and DN determine uniquely values of V_{BP} and V_{BN} respectively. Then we can determine the value of V_B by the relation $\{V_B = EG - V_{out} - V_{BP} - V_{BN};\}$. And finally the depletion width WD is uniquely determined as $\{WD = \sqrt{((2\epsilon_{Si} V_B)/((1/DP)+(1/DN)))};\}$.

When the doping level DN of the surface N-region approaches the limiting value of the state density N_c of the conduction band edge, we have $\{V_{BN} \rightarrow 0;\}$. We have $\{V_B \rightarrow (EG - V_{BP} - V_{out});\}$ since we have the relationship $\{EG = V_{out} + V_B + V_{BN} + V_{BP};\}$.

As shown in Figure 8, when both the doping level DP of the P-type substrate wafer and the doping level DN of the surface N-region approach zero, the barrier potentials V_{BN} and V_{BP} both approach to $EG/2$ respectively. And the sum of the barrier potentials $(V_{BN}+V_{BP})$ approaches the silicon band gap energy EG . we then have $\{V_{out} \rightarrow 0; V_B \rightarrow 0;\}$.

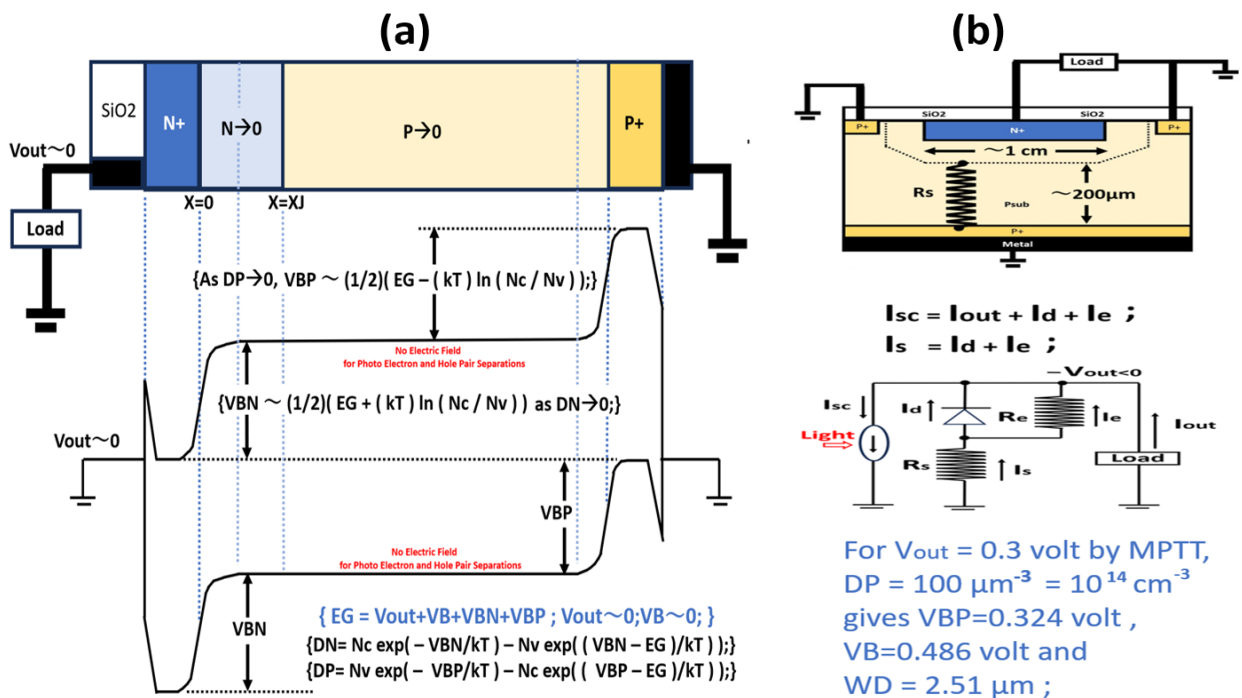


Figure 8. A Floating-Surface N+NPP+ Single Junction Photodiode Solar Cell as $DP \rightarrow 0$ and $DN \rightarrow 0$.

Figure 9 shows various types of photodiodes in comparison for solar cell applications. Figure 9a shows the classical very simple conventional floating-surface NP single junction photo diode, now widely used for solar cell applications with attractive cost-merit and simplicity of fabrications. Figure 9b is the floating-surface N-I-P junction photodiode originally invented by Prof. Jun-ichi Nishizara in

1950s [36–37] which uses an intrinsic semiconductor or an extremely-low-concentration semiconductor wafer resulting in a very large depletion width W_d for effective separations of photo electron and hole pairs.

The surface N regions in Figure 9a,b are floating and suffers undesired serious image lag problem. For intrinsic silicon used in the photodiode shown in Figure 9b, Fermi level E_f approaches to the middle of the silicon band gap. As explained in details later, the external metal-to-semiconductor ohmic contact formation with the intrinsic semiconductor induces an undesired voltage drop, lowering the output voltage. Figure 9c shows a CCD/MOS capacitor type buried channel photodiode with the complete charge transfer capability and the no-image-lag feature. However, the conductive metallic MOS electrode does not pass short-wave blue-light. And the strong surface electric field induces undesired surface dark current. Figure 9d shows the pinned-surface double junction photodiode, which is also completely free from image lag. For high-performance image sensor applications the double junction type shown in Figure 9d is now used.

Historically, Sony explored a variety of sensor structures [38–43] including the CCD/MOS capacitor type for photo image sensing in 1980 while other competing companies used, instead, the simple floating-surface N+P single junction type photodiode shown in Figure 9a. However, structures shown in Figure 9a,b,c all have some undesired demerits of the surface dark current or the image lag.

The pinned-surface P+PNPP+ double junction photodiode shown in Figure 9d has a wide depletion region and also the pinned-surface P+P doping variation both work for effective separations of photo electron and hole pairs and is expected to have a high photon-to-electron conversion efficiency.

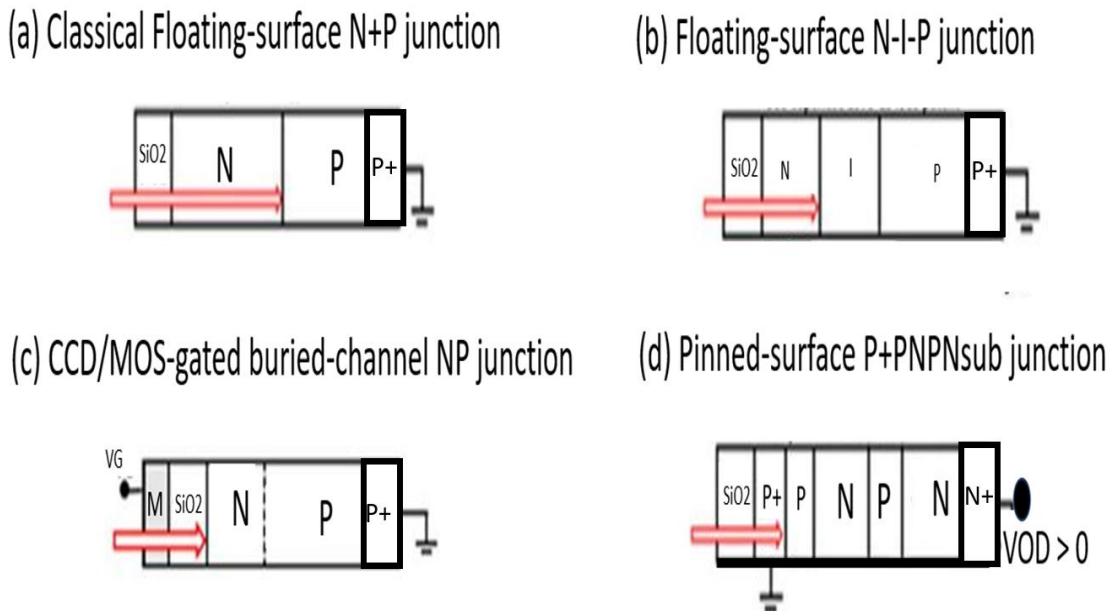
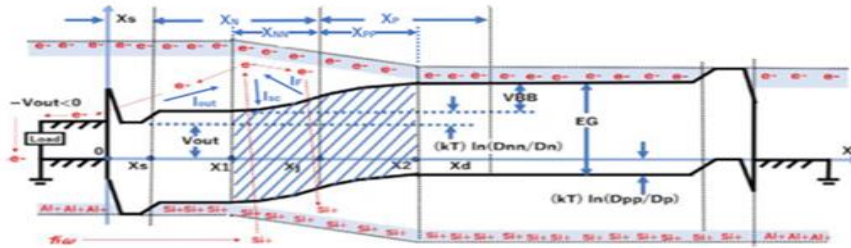


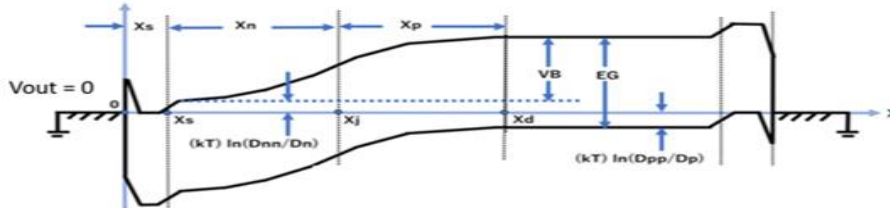
Figure 9. Various types of photo diode structures in comparison for solar cell applications.

Figure 10 shows a combined structure of a small-area N+NPP+ single junction outlet photodiode and a large-area P+PNPP+ double junction photodiode with a wider depletion region for separating effectively photo electron and hole pairs and expecting a higher photon-to-electron conversion efficiency.

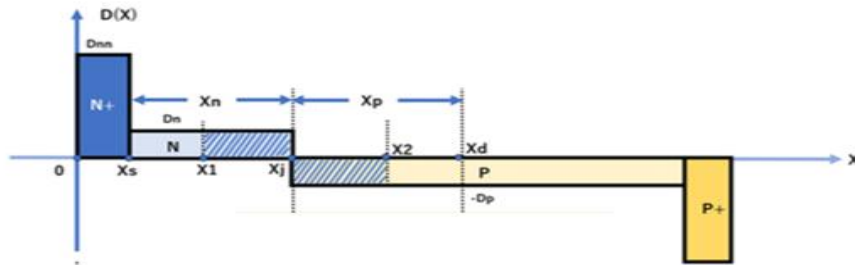
(a) Band Diagram of N+NPP+ Single Junction Photodiode type Solar Cell with $-V_{out} < 0$.



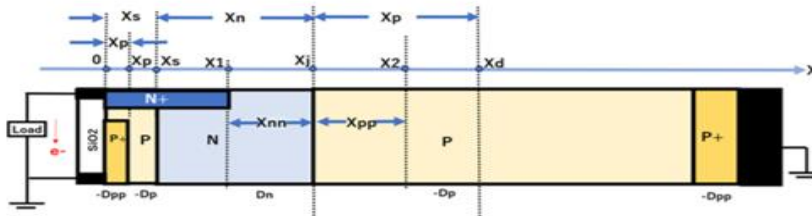
(b) Band Diagram of N+NPP+ Single Junction Photodiode type Solar Cell with $V_{out} = 0$.



(c) Doping Profile $D(X)$ of N+NPP+ Single Junction Photodiode type Solar Cell.



(d) Cross sectional View of Pinned-Surface P+PNPP+ Double Junction Photodiode Solar Cell.



(e) Band Diagram of Pinned-Surface P+PNPP+ Double Junction Photodiode Solar Cell.

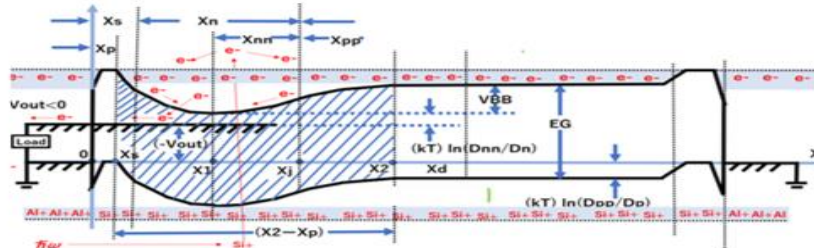


Figure 10. N+NPP+ single junction solar cell and P+PNPP+ double junction solar cell in comparison.

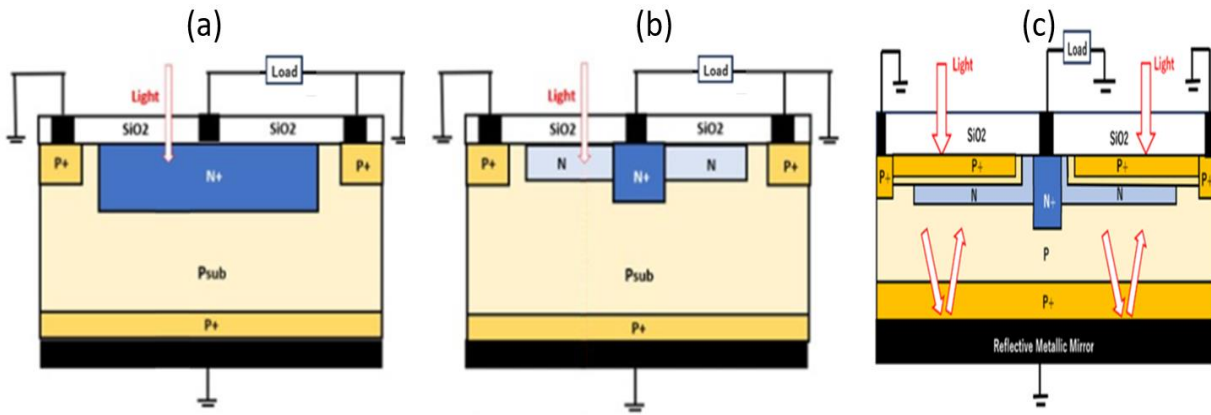


Figure 11. Two types of single junction photodiodes (a) and (b) with a double junction photodiode (c).

Figure 11a shows a floating-surface single junction solar cell with a simple standard four-mask process. Figure 11b shows a five-mask process with an additional high-energy ion implantation for the lightly-doped N region formation. Figure 11c shows a six-mask process for a pinned-surface P+PNPP+ double junction photodiode solar cell with another additional low-energy ion implantation step for forming the surface P+P region. This P+PNPP+ double junction solar cell can be applied not only for the silicon-crystal based solar cell but also for the thin-film amorphous-silicon-based solar cell and also with other base materials such as for the perovskite solar cell. The additional increase in the total production-cost is minimal since only two additional ion implantation steps for the surface P+P formation are needed.

Figure 12a explains conceptually how the large read-out bit-line capacitance is causing the undesired thermal CkT noise in classical old MOS image sensors with floating-surface single-junction photodiodes. Figure 12b shows how a simple N+PsubP+ single-junction photodiode widely applied in classical MOS image sensors suffers the serious image lag problem.

At the reset time, as the photo charge is being drained out of the floating-surface image sensing and storage N+ region thru the charge transfer gate CTG, the potential level V_s of the photo charge sensing and storage region is slowly approaching to the level of the channel potential V_{ch} , which is governed by the current-voltage I/V relationship $\{I_{ds} = I_o (V_s - V_{ch})^2\}$ for the drain current I_{ds} [44–45].

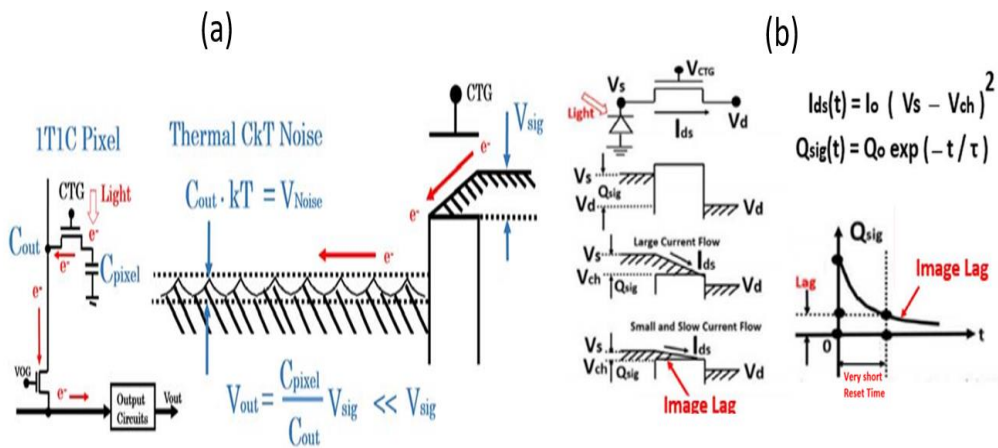


Figure 12. (a) CkT noise and (b) image lag in single junction photodiodes.

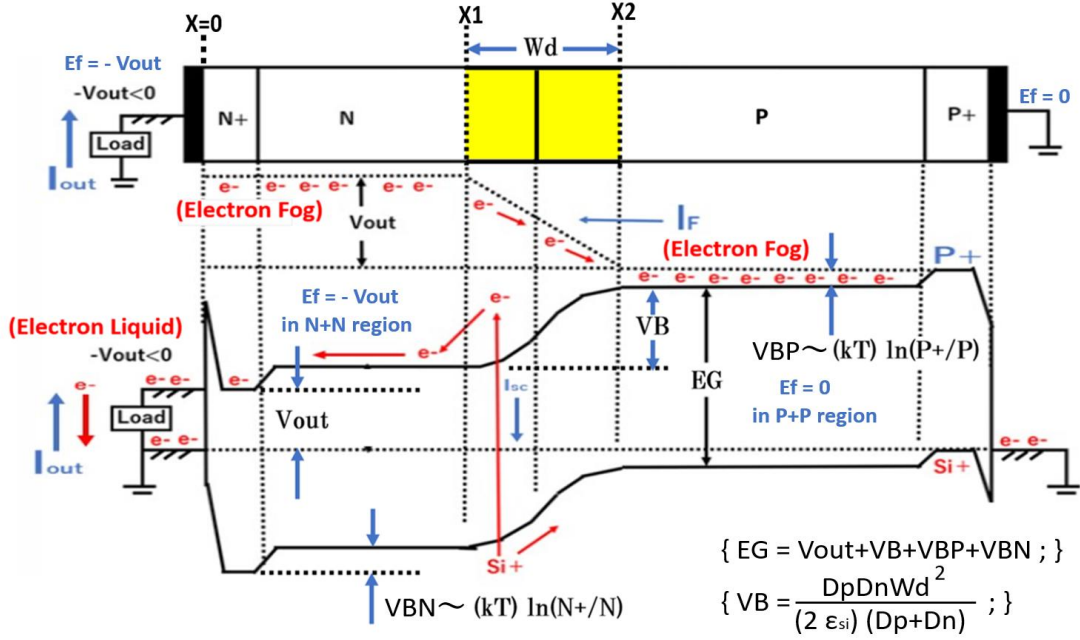


Figure 13. A floating-surface N+NPP+ single-junction photodiode for a solar cell application.

4. The conventional floating-surface N+NPP+ single-junction photodiode-type solar cell

Figure 13 shows a cross-sectional view of a floating-surface N+NPP+ single-junction photodiode for a solar cell application. Fermi level (E_f) is at the ground voltage level in P+ region while in N+ region we have $\{E_f = -V_{out} < 0\}$. Photo electron and hole pairs are generated in the depletion region and separated effectively by the electric field present in the depletion region. The depletion width (WD) can be made wider by lowering the substrate doping level (DP) [46].

However, the backside P+ diffusion region needs to be heavily doped to form a perfect ohmic contact with the backside external metal wiring. The backside P+P doping variation gives the backside P+P barrier potential (VBP). The surface N+N type heavily doped region is needed to achieve an ohmic contact with the surface metal contact region, connecting the solar cell external output load. The surface N+N doping variation gives the surface N+N barrier potential (VBN). We then have the relationship $\{EG = V_{out} + VB + VBN + VBP\}$.

The electron concentration in the N-type region is given as $\{n(x) = N_c \exp((E_c(x) - E_f)/kT)\}$ while the hole concentration in the P-type region is given as $\{p(x) = N_v \exp((E_f - E_v(x))/kT)\}$. We have the effective density of the state at the edge of the conduction energy band as $\{N_c = 1.04 \times 10^{19} \text{ cm}^{-3}\}$ and the effective density of the state at the edge of the valence energy band as $\{N_v = 2.8 \times 10^{19} \text{ cm}^{-3}\}$. In the thermal equilibrium, we have $\{E_c(x) < E_f < E_v(x) ; \rho(x) = p(x) - n(x) + D(x) = 0 ; \}$.

In the P-region, we have $\{E_f = 0 ; E_v(x) = VBP > 0 ; E_c(x) = VBP - EG < 0\}$. And we get the relationship $\{D(x) = -DP = -N_v \exp(-VBP/kT) + N_c \exp((VBP - EG)/kT)\}$ while in the N-region from the relationships $\{E_f = -V_{out} < 0 ; E_v(x) = EG - V_{out} - VBN > 0 ; E_c(x) = -V_{out} - VBN < 0\}$, we have the relationship $\{D(x) = DN = -N_v \exp((VBN - EG)/kT) + N_c \exp(-VBN/kT)\}$. As DN goes zero we have $\{VBP = (EG + kT \ln(N_v/N_c))/2\}$ while $\{VBN = (EG - kT \ln(N_v/N_c))/2\}$ as DN goes zero.

According to the intensity of the solar cell input photo current (I_{sc}), the output voltage (V_{out}) is controlled small, by the maximum power tracking technology (MPTT). Both substrate impurity doping (DP) and depletion width (WD) have some optimum values. In this case, when the maximum power tracking technology (MPTT) controls the output voltage (V_{out}) to be low, the V_B increases, which occurs because the barrier potential for the N+N junction (V_{BN}) and the barrier potential for the P+P junction (V_{BP}) remain unchanged under the equation of $\{E_G = V_{out} + V_B + V_{BN} + V_{BP}\}$.

The solar cell input photocurrent (I_{sc}) also causes a Fermi level difference across the PN junction, leading to a forward biasing of the PN junction and a decrease in the barrier potential of the PN junction (V_B) from that of the thermal equilibrium state.

Figure 14a shows a rain-drop model of floating clouds in a clear sky over a wide-open flat ocean. Clouds are generated by the vaporized water molecules being energized by the strong sunshine in the open sky. If no wind is blowing, the clouds stay where they are born on the ocean and eventually all the rain drops fall back to the ocean again. Figure 14b shows electron-and-hole-pair generation and recombination at the vicinity of the floating-surface N+P single junction photodiode. Figure 14a,b show generation, separation and recombination of electron fog-clouds. Wind is the moving-force for the rainy clouds while electric field is the moving-force for photo electron-and-hole pairs in high-energy vapor-fog state.

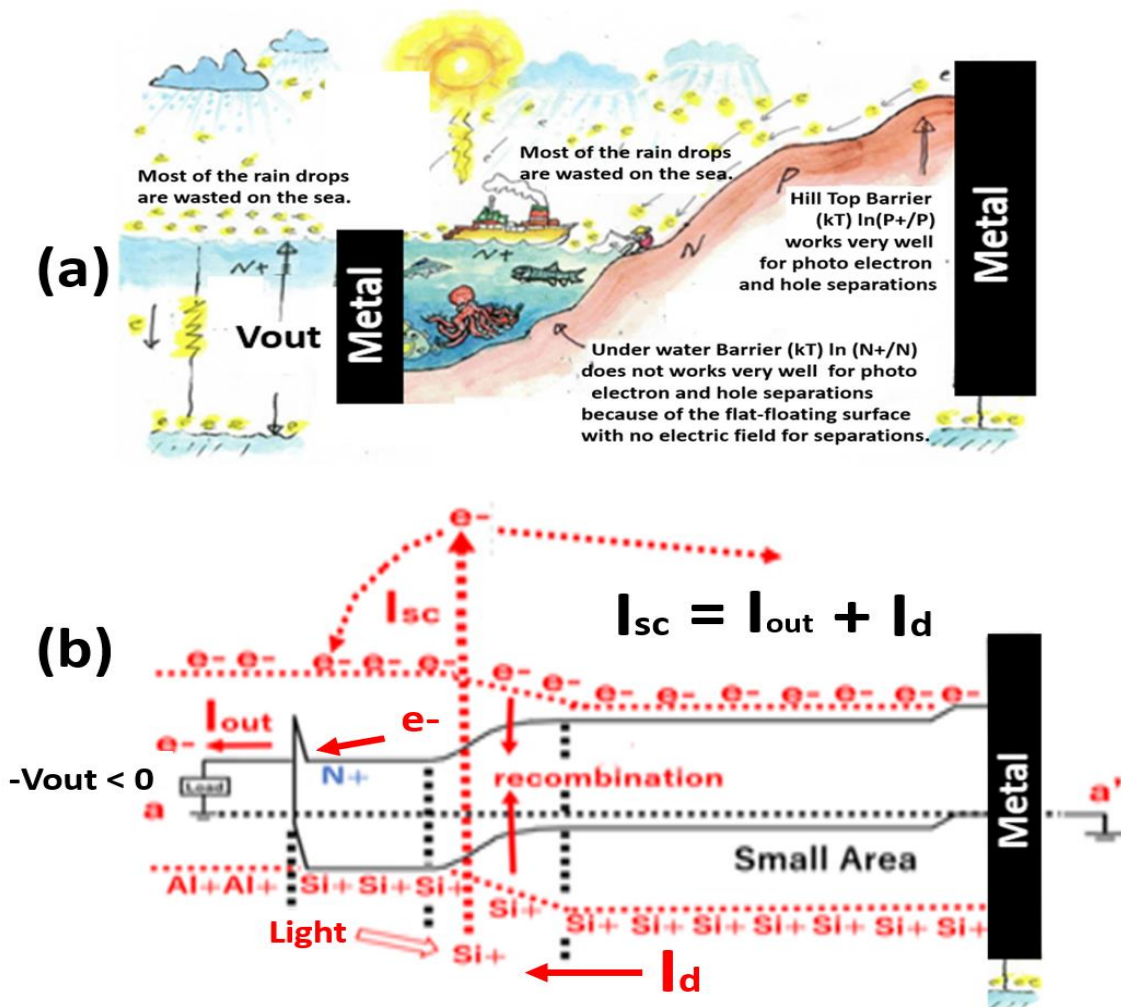


Figure 14. Photo Electron and Hole Pair Generation in N+PP+ Single Junction Solar Cell.

Only the photons reaching inside of the depletion region of the N+P junction can contribute as the solar cell photo current I_{sc} , which is the sum of the forward diode current I_d and the output current I_{out} flowing out from the N+ outlet diffusion region. We have the relationship $\{I_{sc} = I_d + I_{out};\}$ with the output current I_{out} and the output resistance R_{out} $\{I_{out} = V_{out}/R_{out};\}$, where V_{out} is the solar cell output voltage and R_{out} is the effective solar cell output resistance.

The forward photodiode current I_d is due to the high-energy vaporized hot electron fog, while the solar cell output current I_{out} is due to the cooled-down low-energy “liquid” electrons.

By definition, this is the reason why the solar cell power efficiency is lower than the quantum efficiency, which is defined as the ratio of the number of generated photo electrons divided by the number of illuminated photons.

Figure 15a shows a cross sectional view of a wide-area P+PNPP+ double junction photo diode coupled with a small-area conventional N+PP+ single junction photo diode.

Figure 15b shows the band diagram of a pinned-surface P+PNPP+ double junction photodiode for a high performance solar cell application. The cold-temperature “liquid” electrons are collected by the large-area of the middle-centered N-type completed-depleted buried-channel photo electron collector region.

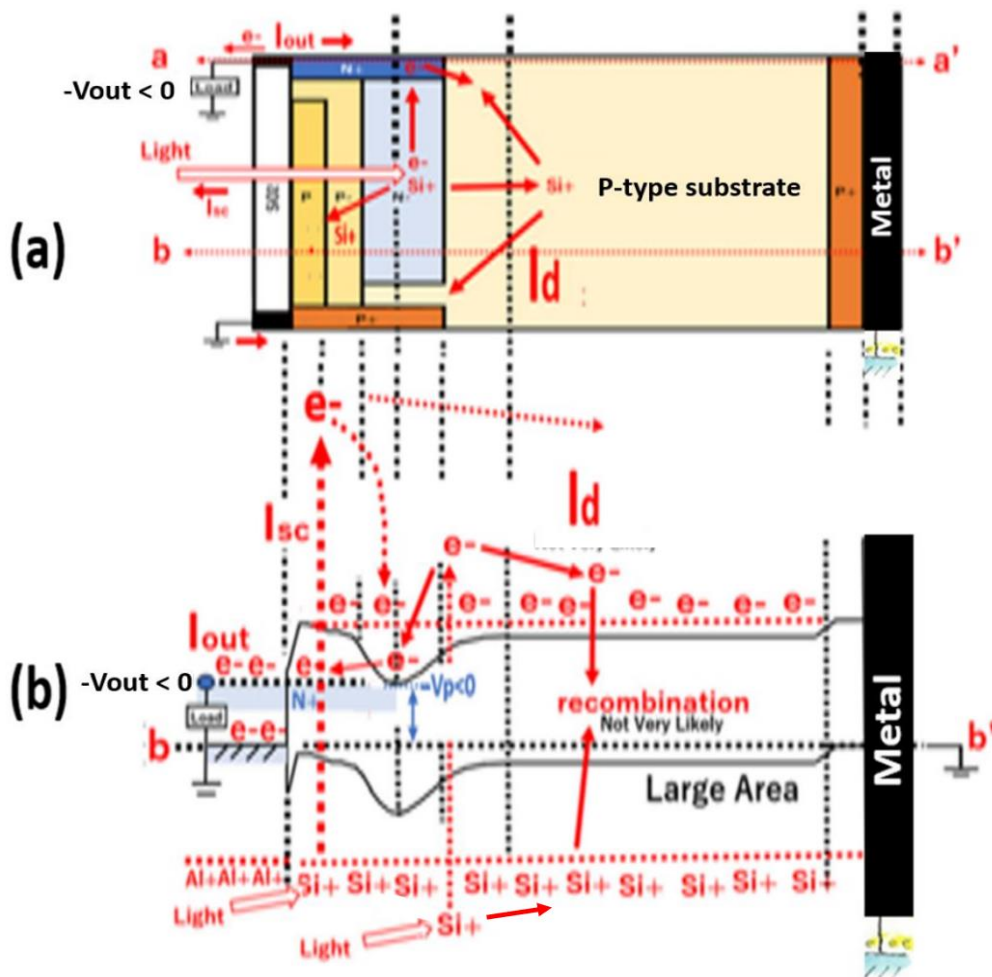


Figure 15. Photo Electron and Hole Pair Generation in P+PNPP+ Double Junction Solar Cell.

5. P+PNPP+ double junction solar cell with pinned-surface and pinned empty-potential-well

For the visible light of the wave length $\{ 0.4 \mu\text{m} < \lambda < 0.7 \mu\text{m}; \}$, silicon crystal looks very metallic dark because it does not pass the visual light with the band gap energy $\{ EG = 1.11 \text{ eV}; \}$, the silicon crystal is transparent for infrared light with wave-length longer than $\{ \lambda_{\text{si}} = 1.24/EG = 1.12 \mu\text{m}; \}$. Short-wave high-energy blue light is absorbed in the vicinity of the silicon surface and wasted as heat in the conventional floating-surface N+NPP+ single junction type solar cell. For the $0.4 \mu\text{m}$ range short wave-length blue-light, we need to devise a way to form the surface barrier electric field for separating the photo electron and hole pairs generated at the vicinity of the silicon crystal surface because the $0.4 \mu\text{m}$ range short wave-length blue-light cannot penetrate deep into the silicon crystal.

Since we have the relationship $\{ D(x) = -DP = -N_v \exp(-VBP/kT) + N_c \exp((VBP - EG)/kT); \}$ in the P-region, the surface conduction band bending (VBP) is created by the surface P+P impurity atom density variation, which is given approximately by $\{ VBP \sim (kT) \ln(P+/P); \}$ for $\{ P+ \sim P; \}$. This surface barrier potential (VBP) creates the surface barrier electric field for effectively separating photo electron and hole pairs generated by the short-wave light at the vicinity of the silicon crystal surface. Figure 16a shows results of numerical computations of actual electron potential profiles with the barrier height VBP created by the surface P+P impurity atom doping variation.

Figure 16b shows the space charge polarization curve and the surface built-in barrier potential profile, generated by the pinned-surface P+P doping variation, by actual numerically-exact computations. The barrier potential VBP, created by the P+P doping variation, was found to be extending from the silicon surface $\{ X = 0; \}$ to more than $1 \mu\text{m}$ depth in silicon $\{ X > 1 \mu\text{m}; \}$, wide enough to separate photo electrons and hole pairs at the silicon pinned-surface P+P region. Since there is no silicon chip yet, which is under preparations, no real data is available for comparison between the conventional and the proposed double-junction solar cells. Expected results will be published as soon as the silicon chip is fabricated.

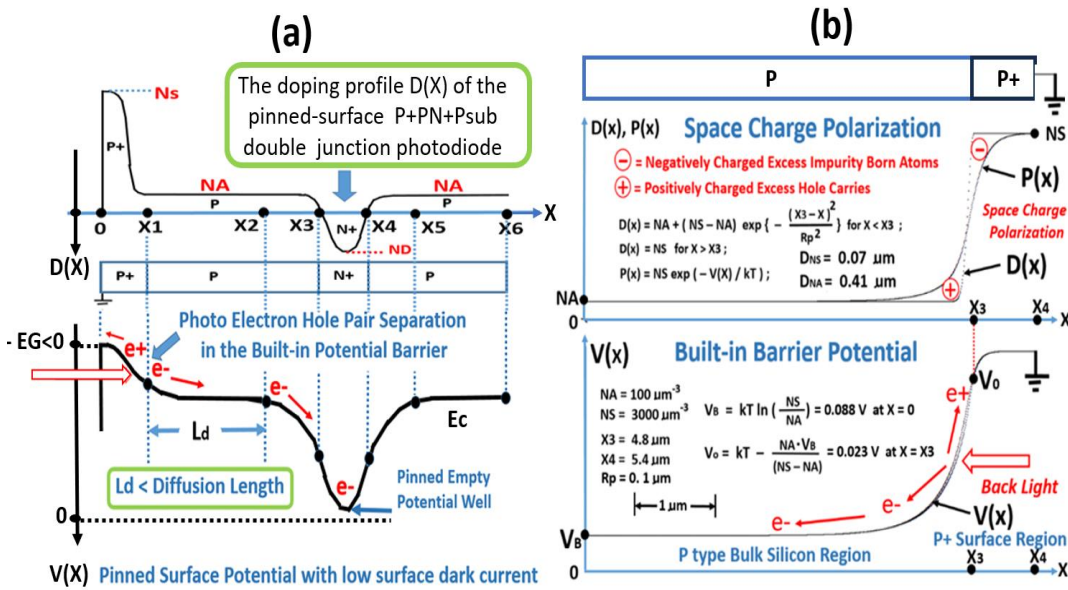


Figure 16. Surface Potential Barrier $VBP = (kT) \ln (P+/P)$ in P+PNPP+ Double Junction Photodiode.

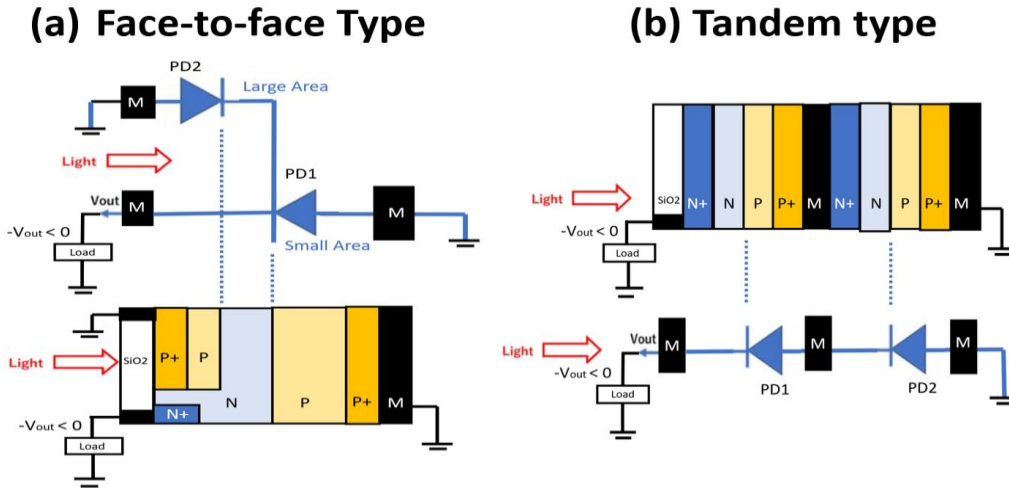


Figure 17. Two types of Double Junction Solar Cells in comparison.

Figure 17 shows two types of configurations for double junction solar cells. The P+PNPP+ double junction photodiode shown in Figure 17a has the P+PNPP+ doping profile, which is symmetric at the middle-point, centered by the buried-channel N region with a symmetric pinned empty potential well. Hence, we expect a wider and doubled depletion width $\{W_d = [X_1, X_2];\}$ for the pinned-surface P+PNPP+ double junction pinned photo diode. The pinned-surface P+ hole accumulation regions both in the surface and the backside create the surface P+P barrier potential $\{V_{BP} \sim kT \ln (P+/P);\}$ for $\{N_v \sim P+ < P;\}$, as governed by the relationship $\{DP = N_v \exp (- V_{BP}/kT) - N_c \exp ((V_{BP} - EG)/kT);\}$, which gives $\{V_{BP} \rightarrow EG/2;\}$ as the substrate doping DP gets very low.

Both at the surface and the backside P+P impurity doping variations give a barrier potential VBP, separating effectively the minority carrier photo electron and hole pairs in the P+P pinned-surface heavily-doped hole-accumulation regions while majority carrier holes both at the front surface region and the back surface region see only the flat sea of hole majority carriers with no moving force.

Figure 17b shows two N+NPP+ single photodiodes connected with a metallic ohmic contact region in-between in tandem formation [47]. The structure looks very complex and costly with the extra metallic region in-between. The N+NPP+ single junction type solar cell is a simple, low-cost and very attractive. However, the double-junction tandem solar cell needs an undesired metallic ohmic bridging-layer in-between. For the triple junction tandem solar cell, we need two extra undesired metallic ohmic bridging-layers in-between.

In order to have good ohmic contacts with the undesired metallic bridging-layers, for each N+NPP+ single junction photodiode, the heavily doped N+ and P+ regions are needed. However, the P+P and N+N variation induced barrier potentials VBP and VBN both decrease the magnitude of the output voltage Vout since we have $\{V_{out} = EG - V_B - V_{BP} - V_{BN};\}$. A single PN junction depletion width (Wd) is computed by the relationship $\{V_B = W_d^2 * DP / (2\epsilon_{si});\}$ and $\{W_d = \sqrt{2\epsilon_{si} V_B / DP};\}$. The width (WD) of the depletion region needs to be kept wide enough for effectively separations of the photo electron and hole pairs in the NP junction depletion region in order to achieve a good solar cell efficiency.

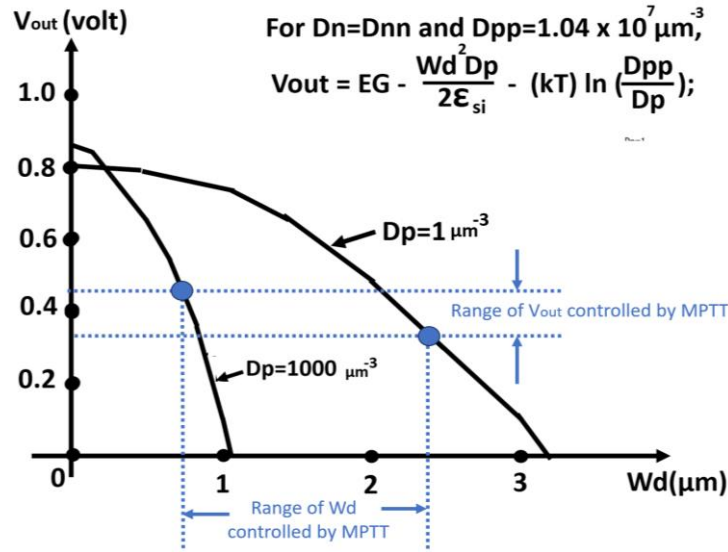


Figure 18. Expected Output Voltage V_{out} of Floating-Surface N+PP+ Single Junction Solar Cell.

However, these barrier potentials V_{BP} and V_{BN} give the undesired effects of minimizing the output voltage V_{out} , which is governed by the relationship $\{V_{out} = EG - V_B - V_{BN} - V_{BP} > 0\}$. Using the depletion width W_d as an independent variable and the p-type substrate doping level DP as another independent parameter, we can now compute the values of the solar cell output voltage V_{out} , using the relationship $\{V_{out} = EG - V_B - V_{BN} - V_{BP} > 0\}$.

Figure 18 shows the values of the output voltage V_{out} , which is computed and plotted along the Y-axis, as a function of the depletion width W_d , taken along the X-axis, with an independent parameter of the substrate doping level DP . Two extreme cases with values $\{DP = 1 \mu\text{m}^{-3}$ and $DP = 1000 \mu\text{m}^{-3}\}$ are shown in the simplified case with the condition $\{D(X) = D_N \rightarrow N+\}$. The output voltage V_{out} is found to be centered around $\{V_{out} \sim 0.4 \text{ volt}\}$, and we have $[0.7 \mu\text{m} < W_d < 2.4 \mu\text{m}]$.

6. The conditions to obtain the maximum power in the N+NPP+ single-junction photodiode

The total internal solar cell photo current I_{sc} is generated according to the intensity of the illuminated sun light. For the case of a floating-surface N+NPP+ single-junction type photo diode, we have the relationship (1) $\{I_{sc} = I_{out} + I_d\}$. The output current I_{out} and the forward-biased current I_d shares the solar cell current I_{sc} . However, for the case of the pinned-surface P+PNPP+ double junction, we have another surface-side photodiode current I_{ds} which also shares the solar cell photo current I_{sc} . And we have the relationship (1a) $\{I_{sc} = I_{out} + I_d + I_{ds}\}$. The output power of the solar cell is simply given as the product $\{\text{Power} = (I_{out})(V_{out})\}$.

The photodiode forward current I_d is given as (2) $\{I_d = I_o (\exp(V_{out} + V_s)/kT) - 1\}$ where the constant $\{I_o = A_o \exp(-EG/kT)\}$ is depending on the size (A_o) of solar cell photodiode. The N+NPP+ single-junction photodiode with the output voltage of $\{(- V_{out}) < 0\}$ becomes forward biased as the intensity of the sun light illumination increases. We also have the relationship between the substrate resistance R_s and the undesired voltage drop V_s as (3) $\{V_s = R_s \times I_d > 0\}$.

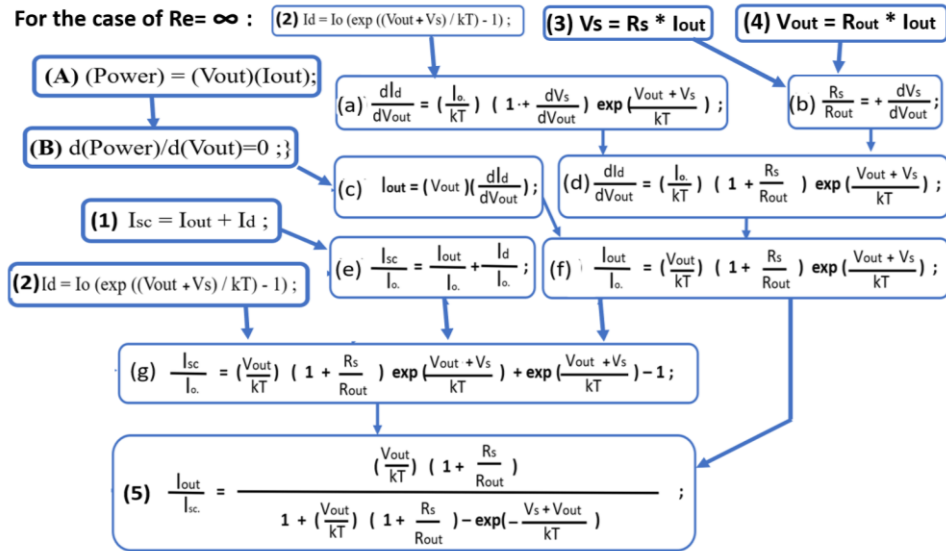


Figure 19. A flow chart of a salient computational algorithm to obtain the value of (Iout/Isc).

The optimum value of the effective output resistance R_{out} is controlled for the maximum solar cell power point, by the maximum power tracking technology (MPTT) [48–49]. The output current I_{out} and the output voltage are related as (4) $\{V_{out} = I_{out} \times R_{out}$; or $R_{out} = V_{out}/I_{out}\}$.

Since the solar cell power is defined as (A) $\{\text{Power} = (V_{out})(I_{out})\}$; and for the maximum power point, by solving the differential equation (B) $\{d(\text{Power}) / d(V_{out}) = 0\}$; we obtain the output current (I_{out}/I_{sc}) (5) $\{(I_{out}/I_{sc}) = (V_{out}/kT) (1 + R_s/R_{out}) / (1 + (V_{out}/kT) (1 + R_s/R_{out}) - \exp(- (V_s + V_{out})/kT))\}$ as a function of the parameters $\{V_{out}/kT$ and $R_s/R_{out}\}$.

Using relationships (1) thru (4), the complex algorithm chart for the mathematical computation as shown in Figure 19, gives the ratio (I_{out}/I_{sc}) of the output current I_{sc} divided by the photo current I_{sc} . From the relationship (5), for the simple case of the zero-substrate resistance $\{R_s = 0\}$; we have the output current (I_{out}/I_{sc}) as (6) $\{(I_{out}/I_{sc}) = (V_{out}/kT) / (1 + (V_{out}/kT) - \exp(- V_{out})/kT)\}$. See Figure 20.

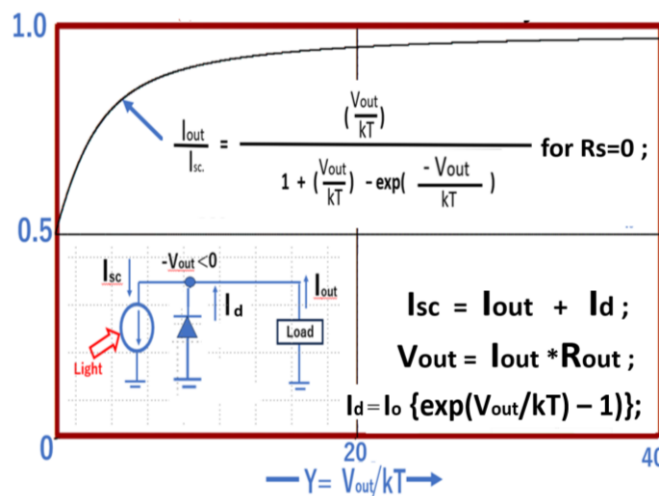


Figure 20. The dependence of the output current I_{out} upon V_{out} for the case of $R_s=0$.

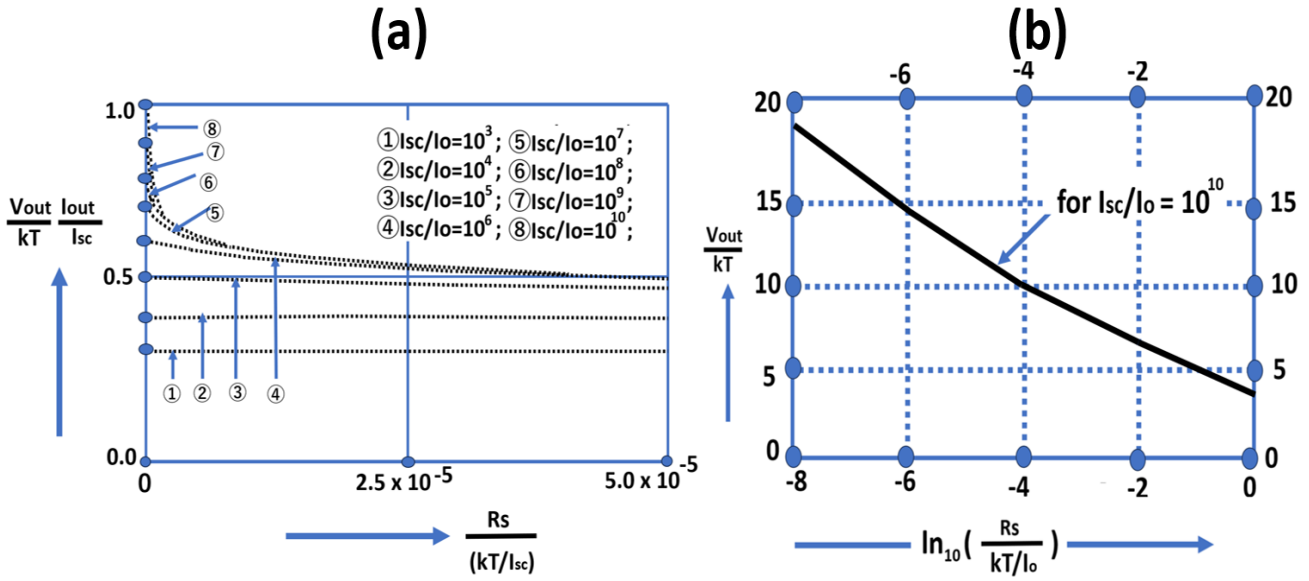


Figure 21. The dependence of the power and the output voltage upon the substrate resistance R_s .

7. The dependence of the solar cell output power upon the substrate resistance R_s

For the special ideal case of the zero-substrate resistance $\{R_s = 0\}$, the value of I_{out}/I_{sc} changes from 50% to 100% while the output voltage (V_{out}/kT) increases from zero to $\{EG/kT = 42.9\}$ where we have the values of the silicon band gap energy $\{EG = 1.11 \text{ eV}\}$ and the thermal energy $\{kT = 0.0259 \text{ eV}\}$.

The solar cell photodiode (I_{sc}/I_o) and the substrate resistance R_s are the two external independent parameters. The value of I_{out}/I_{sc} is controlled fairly well with a very small variation in the range between 50% and 100%.

Three parameters, (I_{out}/I_{sc}) , $(V_{out}/kT)(I_{out}/I_{sc})$ and $(V_{out}/kT) / (I_{out}/I_{sc})$, are physical parameters normalized by the solar cell photo current I_{sc} and the thermal energy kT . Their values are well controlled and do not change much. See Figure 21a.

Figure 21b shows the dependence of the output voltage V_{out}/kT upon the magnitude of the normalized substrate resistance $(R_s \times I_o/kT)$. The magnitude of the substrate resistance R_s has a strong undesired effect of decreasing the output voltage (V_{out}/kT) significantly. The DC-to-DC converter technology is widely applied to raise the solar cell output voltage V_{out} . The small value of the solar cell output voltage V_{out} is not very much welcomed in practice.

The substrate resistance R_s and the solar cell photo current I_{sc} are two independent uncontrollable parameters. By a wise scheme of Maximum Power Tracking Technology (MPTT), the output resistance R_{out} and the low output voltage V_{out} are controlled at a fairly-controlled low level.

With the five basic relationships governing the solar cell performance, as explained below, the values of the five basic important physical parameters $\{I_d, V_s, R_{out}, V_{out}$ and $I_{out}\}$ are uniquely determined numerically from the values of the two independent input physical parameters $\{R_s$ and $I_{sc}\}$.

There are the same number of the governing Equations (1) thru (5) shown below with the five unknown parameters $\{I_d, V_s, R_{out}, V_{out}$ and $I_{out}\}$.

The computational algorithm is as followed: Set $\{I_{out} = I_{sc}/2;\}$. And follow the steps shown below and repeat the iterations.

Step (1): get I_d from (1) $\{I_{sc} = I_{out} + I_d;\}$. Step (2): get V_s From (3) $\{V_s = R_s \times I_d;\}$. Step (3): get the value of V_{out} from (2) $\{I_d = I_o (\exp ((V_{out} - V_s) / kT) - 1) ;\}$. Step (4): get the value of R_{out} form (4) $\{V_{out} = I_{out} \times R_{out};\}$. Then we get a new value of the output current I_{out} from the next step defined as Step (5): $\{(I_{out}/I_{sc}) = (V_{out}/kT) (1 + R_s/R_{out}) / (1 + (V_{out}/kT) (1 + R_s/R_{out}) - \exp ((V_s - V_{out})/kT));\}$.

And then return to the Step (1) until we get the final exact values $\{I_d, V_s, R_{out}$ and $I_{out};\}$. By repeating the iteration steps $\{(1) \rightarrow (3) \rightarrow (2) \rightarrow (4) \rightarrow (5) \rightarrow (1);\}$ sufficient times, we get the final values of the five unknown parameters $\{I_d, V_s, R_{out}$ and $I_{out};\}$ as shown in Figure 20 and Figure 21 above.

Figure 22 shows another possible future solar cell application of a multi-junction type pinned-surface and buried-channel type photodiode with the pinned-surface P+P doping variation and the fully-depleted buried N-/P- multi-junction regions. The backside substrate is also pinned by the heavily doped back-side P+ region to form a perfect ohmic contact in the backside with the external metal wiring. This structure is suited for multi-junction thin-film solar cells such as amorphous-silicon and perovskite types.

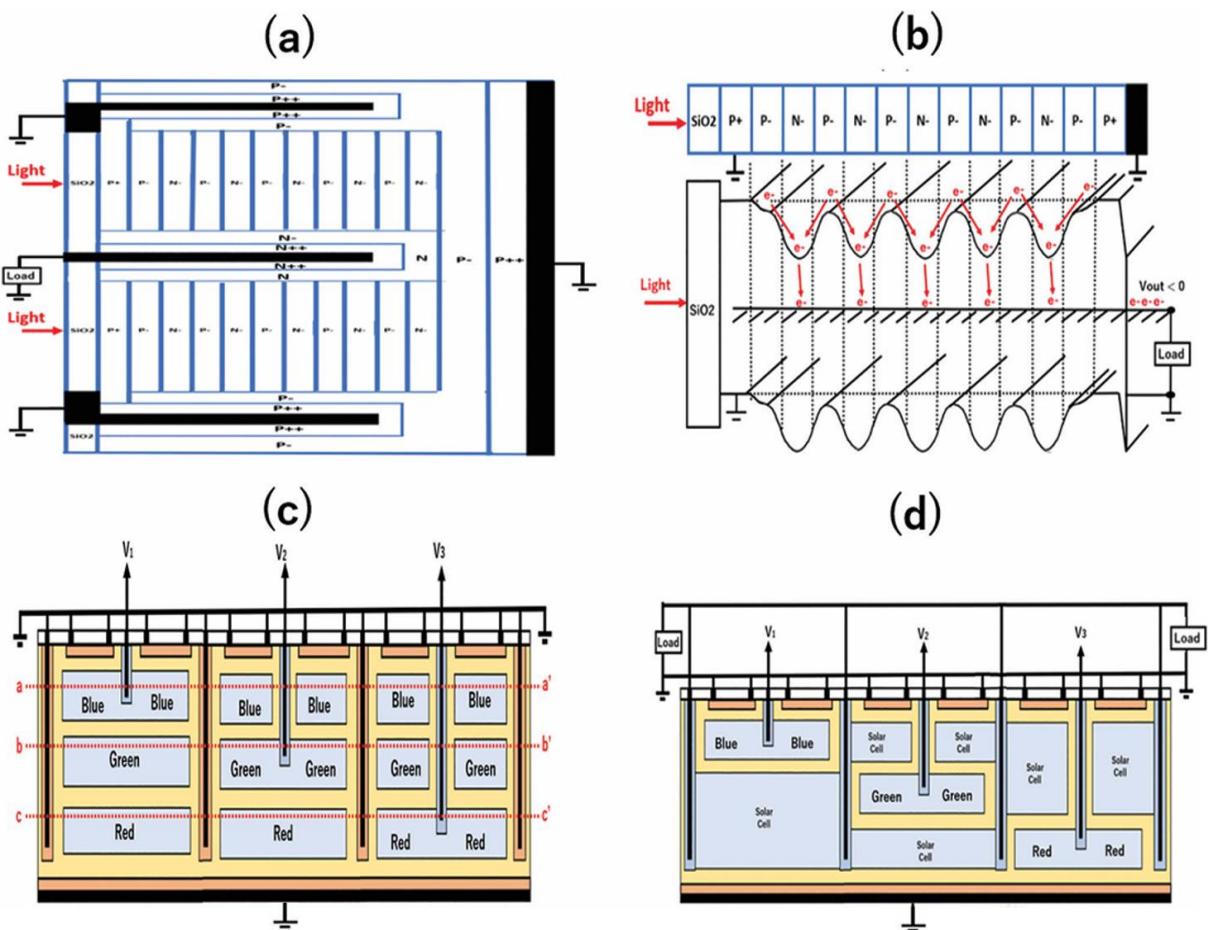


Figure 22 P+PNPN~PNPP+ multi-junction and multi-layer face-to-face type solar cell [13].

8. Photon-to-electron conversion efficiency of the single junction type solar cell

There are three statistical distribution functions, (1) the Maxwell-Boltzmann statistics for identical and distinguishable particles, (2) Bose-Einstein for identical and indistinguishable particles that do not obey exclusive principle and (3) Fermi-Dirac for identical and distinguishable particles that obey the exclusion principle.

A photon gas in a cavity also behaves as electro-magnetic waves like the harmonic oscillators in the cavity, which is subject to Bose-Einstein statistics. For photon gas, the Bose-Einstein distribution function $F_{BE}(f)$ is applicable [50–52]. The frequency f is related by the speed of light c as $\{c = f \lambda\}$. A photon gas in a cavity is governed by the relationship $\{ F_{BE}(f) df = 8\pi h f^3 df / (\exp(hf / kT) - 1) \}$.

Figure 23a shows the widely-known measured data of the sun light power density spectrum $S(\lambda)$ at the sea level as a function of the wave length (λ) of the illuminated sun light along the X-axis [53]. Only photons with the energy greater than the silicon band gap energy of $\{EG = 1.11 \text{ eV}\}$ can contribute to the photon-to-electron energy conversion efficiency. The percentage (%) of the illuminated light with the photon energy density $S(\lambda)$ decreases drastically for the short-wave blue-light photon of the wave length less than about $\{\lambda = 0.4 \mu\text{m}\}$; }.

Figure 23b shows the photon number density $N(\lambda)$ of the sun light illuminated at the sea level, which is computed from the sun light power density spectrum $S(\lambda)$ by the relationship $\{S(\lambda) = (hf) N(\lambda)\}$; and using the basic relationships $\{\lambda(\mu\text{m}) = hc/E_G(\text{eV}) = 1.24/E_G(\text{eV})\}$; $c = f\lambda$; $hf = hc/\lambda$; }.

In 1960s, these data were not available and Shockley used this black body radiation model and considered the sun as a black body [54]. Shockley used a black body radiation model and considered the sun as a black body of the 6000 Kelvin, which gives the thermal energy of $\{kT = 0.517 \text{ eV}\}$; }.

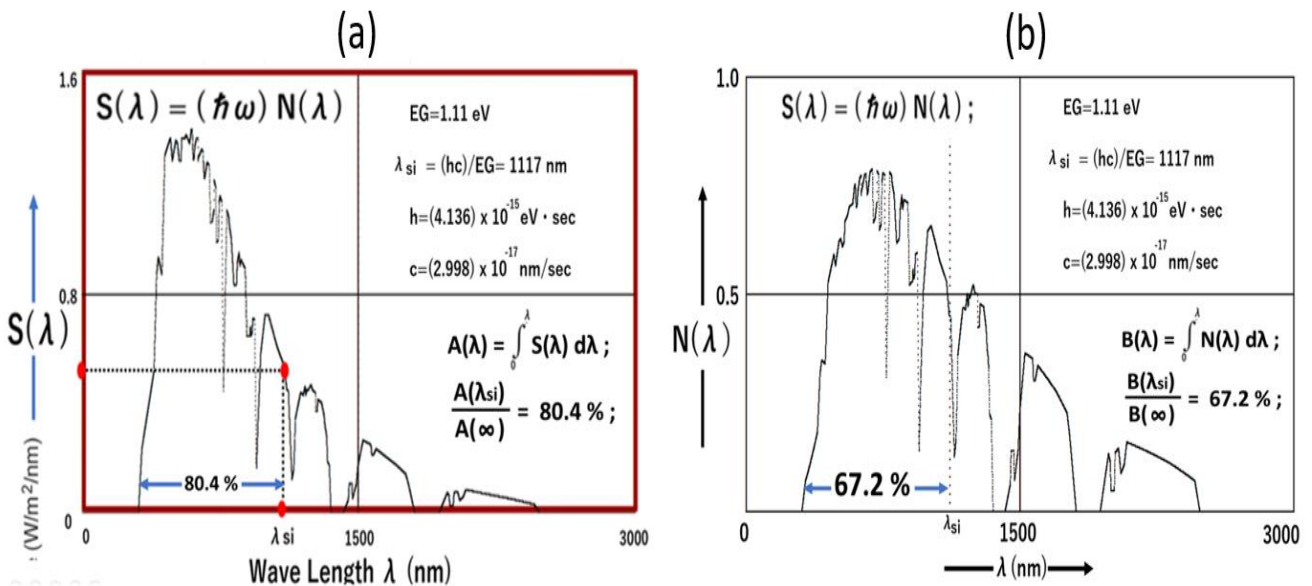


Figure 23. (a)Sun-light power density $S(\lambda)$ [53] and (b)the photon number density $N(\lambda)$.

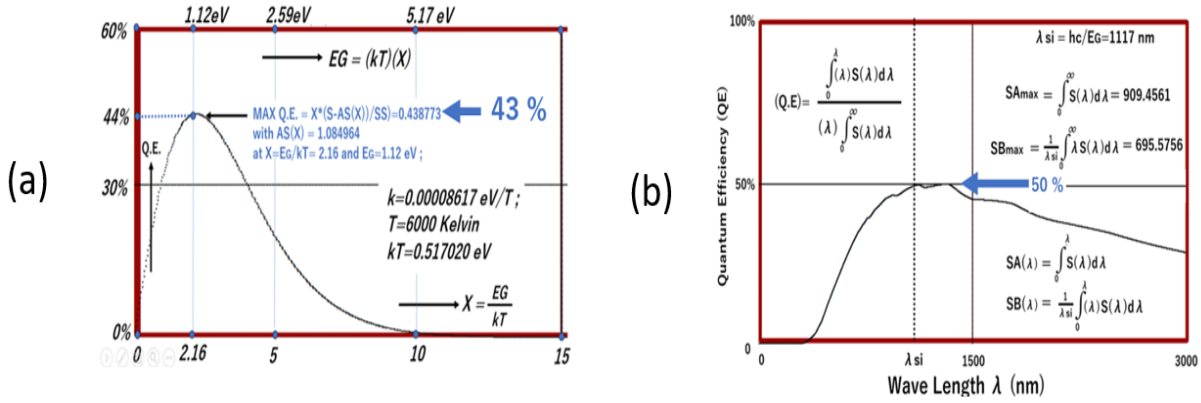


Figure 24. Energy efficiency (a) by black body radiation model and (b) by actual measurement.

He reported the theoretical upper limit 43% of the quantum efficiency (QE), the percentage (%) of the conversion ratio of the photon number to the electron number in a floating-surface N+P single junction type solar cell. See Figure 24a. Now accurate experimental data are available and Figure 24b shows the quantum efficiency as a function of the photon wave length (λ).

9. Percentage (%) of photon numbers penetrating the silicon crystal of arbitrary thickness

For photons with a long wave length λ more than $\{\lambda = 1.117 \mu\text{m};\}$, the silicon crystal is transparent. The entire depletion region $[Wd = [X1, X2];\}$ becomes a transparent region for a photon with a long wave length. About $\{T_1 = 95\%\};\}$ of photons with wave length greater than $\{\lambda_1 = 0.8 \mu\text{m};\}$ pass thru the silicon crystal of thickness $\{X_1 = 0.56 \mu\text{m};\}$ while about $\{T_1 = 37\%\};\}$ of photons with the wave length greater than $\{\lambda_1 = 0.5 \mu\text{m};\}$ pass thru the silicon crystal of thickness $\{X_1 = 0.56 \mu\text{m};\}$.

From the two points data [55], as shown in Figure 25, any percentage $T_\lambda(X)$ of the photon number passing thru at any depth $X(\mu\text{m})$ can be estimated for any wave length $\lambda(\mu\text{m})$.

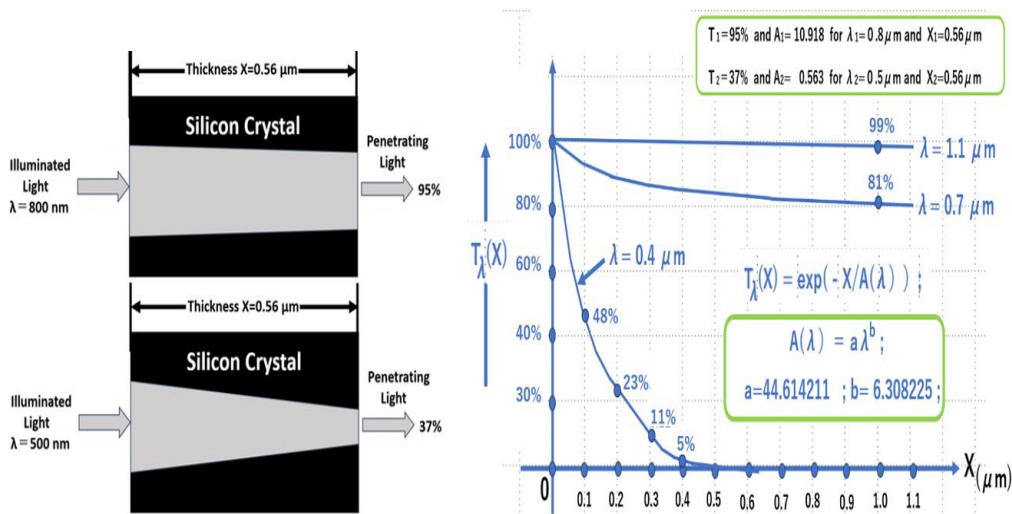


Figure 25. Percentage (%) of photons penetrating in the depth $X(\mu\text{m})$ in silicon crystal [55].

From the two-point measured data, the values of the unknown parameters $\{a \text{ and } b;\}$ for the function $\{A(\lambda) = a\lambda^b;\}$ can be estimated. Then values of the model function $\{T_\lambda(X) = \exp(-X/A(\lambda));\}$ can be

computed. And as shown in Figure 26, the sun-light power spectrum $\{Y_x(\lambda) = S(\lambda) \exp(-X/A(\lambda));\}$ is computed as a function of the photon wave length λ with the silicon-crystal depth X as a parameter. Figure 26a shows the sun light power spectrum $Y_x(\lambda)$ for depth $\{X=0, 0.1 \mu\text{m and } 0.2 \mu\text{m};\}$. And Figure 26b is for the silicon crystal depth $\{X=0.5\mu\text{m and } 1.0 \mu\text{m};\}$.

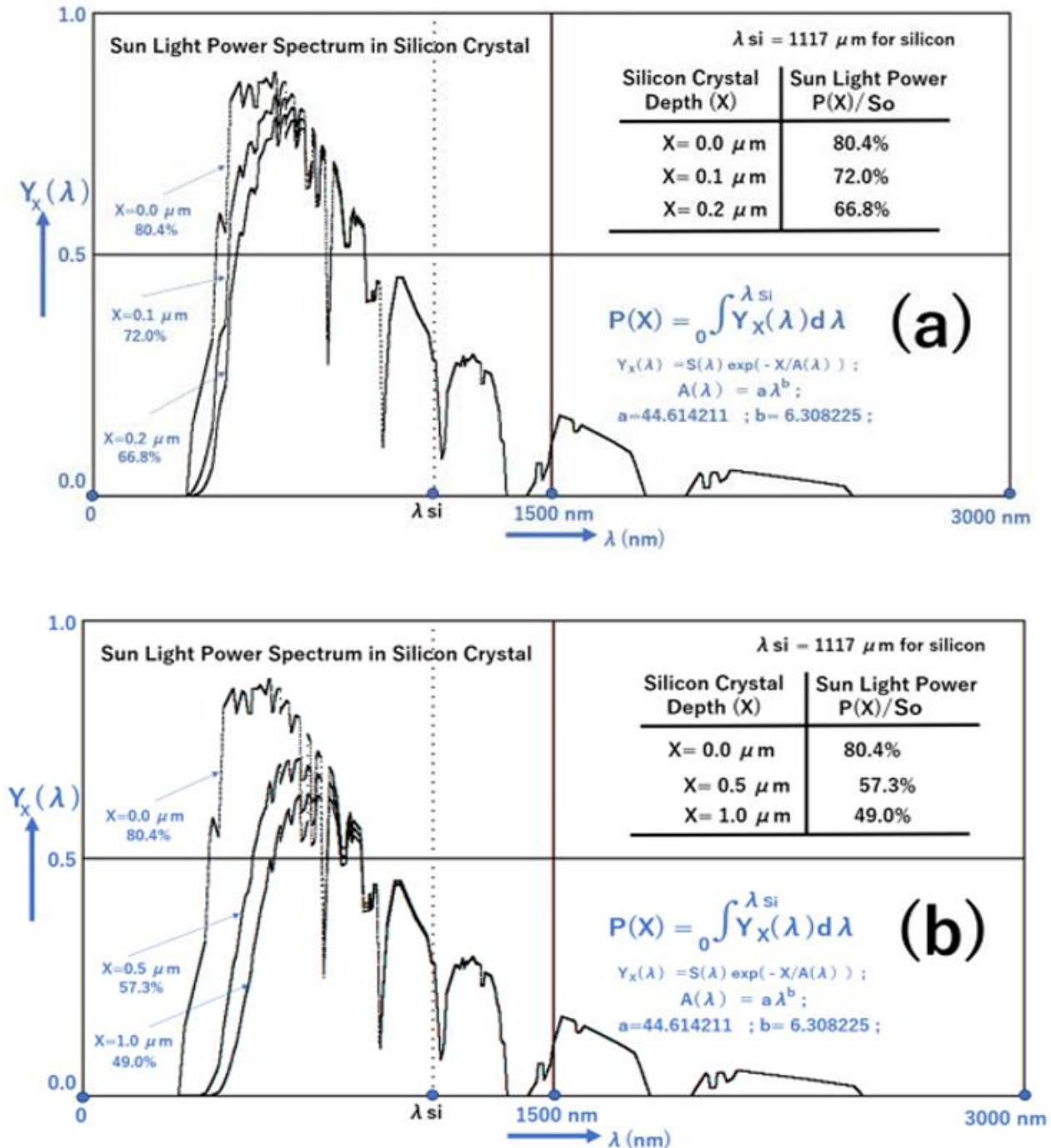


Figure 26 (a) and (b) Sun-light Power Spectrum penetrating at the silicon crystal depth X as a parameter.

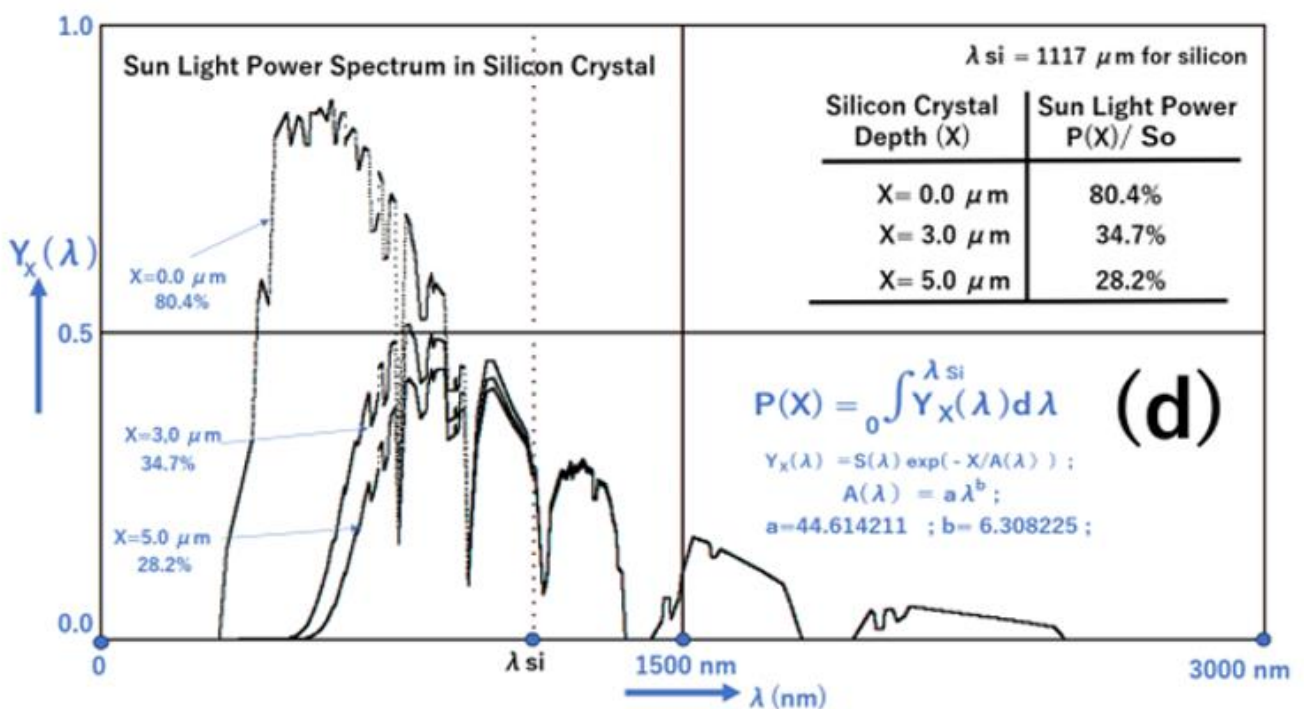
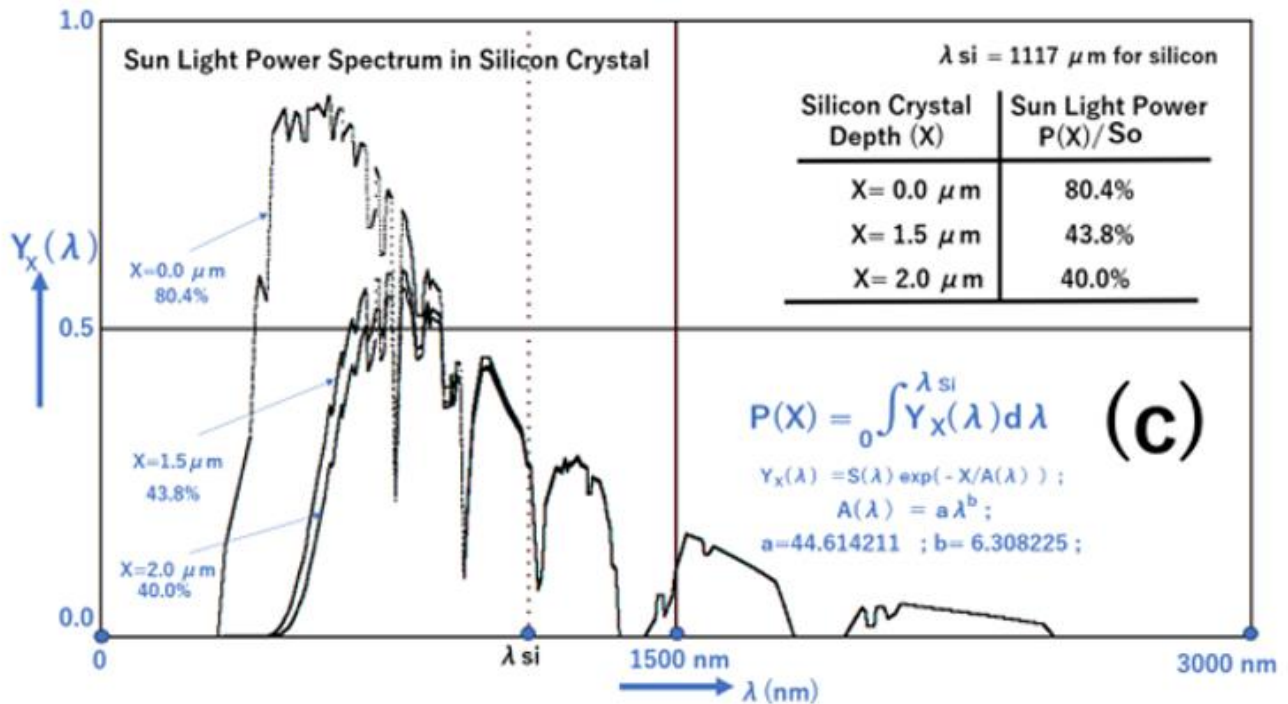


Figure 26 (c) and (d) Sun-light Power Spectrum penetrating at the silicon crystal depth X as a parameter.

Figure 26c is for the silicon crystal depth {X=1.5 μm and 2.0 μm ;}. And Figure 26d is for the silicon crystal depth {X=3.0 μm and 5.0 μm ;}.

10. Percentage (%) of sun-light power penetrating thru silicon crystal depth X(μm)

For photons with the energy less than the semiconductor band gap energy, the semiconductor material itself looks transparent and the photons pass thru the semiconductor material of any substrate thickness.

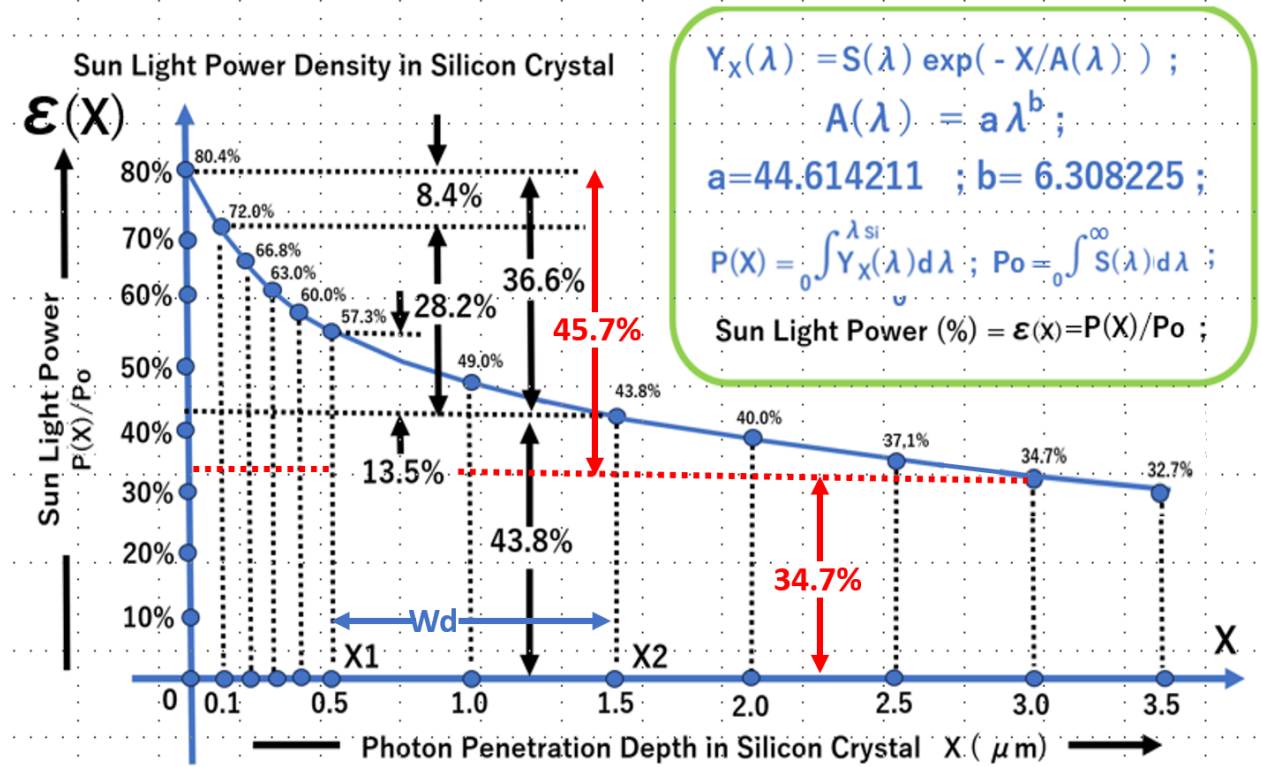


Figure 27. The sun-light power percentage $\epsilon(X)$ penetrating thru silicon crystal at the depth X (μm)

Only 80.4% of the sun light power at the silicon surface $\{X = 0;\}$ can be absorbed theoretically into the silicon crystal and become heat or useful electron energy. The remaining 19.6% of the illuminated sun light photons have the energy less than the silicon crystal band gap energy, and the silicon crystal looks completely transparent. $S(\lambda)$ is the sun-light power spectrum at the silicon surface $\{X = 0;\}$.

Penetrating thru the silicon crystal, the sun-light power spectrum decreases at the silicon crystal depth X with the factor $\{ T_\lambda(X) = \exp(-X/A(\lambda))$ with $A(\lambda) = a\lambda^b;\}$. Figure 27 shows the dependence of the total sun-light power as a function of the silicon crystal depth (X) obtained using the results shown in Figure 26. The sunlight power percentage $\epsilon(X)$, penetrating the silicon crystal at the silicon crystal depth X , can be computed by integrating the product given as $\{ S(\lambda) T_\lambda(X)$ for $\lambda = 0$ to $\lambda = \infty;\}$.

For example, for the depletion region width $\{Wd = \{X1, X2;\};\}$ with $\{X1 = 0.5 \mu\text{m}$ and $X2 = 1.5 \mu\text{m};\}$, we have the penetrating light power as $\{P(X)/So = 57.3\%;\}$ while we have the penetrating light power as $\{P(X)/So = 43.8\%;\}$ for the silicon depth $\{X2=1.5 \mu\text{m};\}$. This figure is the most important computational result which explains why the single-junction type photodiode with a typical depletion width $\{Wd = [X1, X2] = [0.5, 1.5];\}$ has only 13.5% efficiency.

Most of the long-wave photons more than 43.8% are passing thru the single junction depletion region and reaching deep in the silicon crystal substrate where there is no electric field for separating photo electron and hole pairs. The pinned-surface P+PNPP+ double junction photodiode has the pinned-surface P+P doping variation with the surface barrier field that enhances at the silicon surface at $\{X=0;\}$ the photo electron and hole effective pair separations.

For $\{X1 = 0;\}$, the depletion width $\{Wd = [0, 1.5];\}$ gives 36.6% efficiency. By high-energy ion implantation technology, the efficiency of $\{80.4 - 34.7 = 45.7\%;\}$ is also possible, achieving the effective depth of $\{X2 = 3.0 \mu\text{m};\}$. Besides, if we can realize an extremely wide and deep depletion

width with $\{X2 = \infty\}$, with the thin-film multi PN junction structure in an amorphous silicon-based solar cell in the future advance technology, we would have the limiting efficiency of 80.4%.

11. Maximum Power Tracking Technology (MPTT) to extract Maximum Solar Cell Power

The governing relationships are given as $\{V_{out} = E_G - BV - BV_n - BV_p > 0\}$; with the barrier potential V_B given as $\{V_B = Wd^2 \times D_p / (2\epsilon_{si})\}$; for the N+NPP+ single junction photodiode with the floating-surface N+N doping-variation-induced barrier potential given as $\{V_{Bn} = (kT) \ln(D_{nn}/D_n)\}$; and the heavily-doped-substrate ohmic-contact P+P doping-variation induced one as $\{V_{Bp} = (kT) \ln(D_{pp}/D_p)\}$. The solar cell output voltage V_{out} is controlled by the maximum power tracking technology (MPTT) scheme according to the intensity of the illuminated sun light, which determines the solar cell output current I_{sc} as an independent parameter. The external MPTT control system optimizes the output voltage by keeping the PN junction depletion width Wd at an optimum value for the effective photo electron and hole pair separations in order to achieve the maximum power $\{Power = (V_{out})(I_{out})\}$ for the solar cell. By calculating the equation given by relationship $\{d(Power)/d(V_{out}) = 0\}$, we obtain the optimum values of V_{out} and I_{out} and then the value of the load resistance $\{R_{out} = V_{out} / I_{out}\}$.

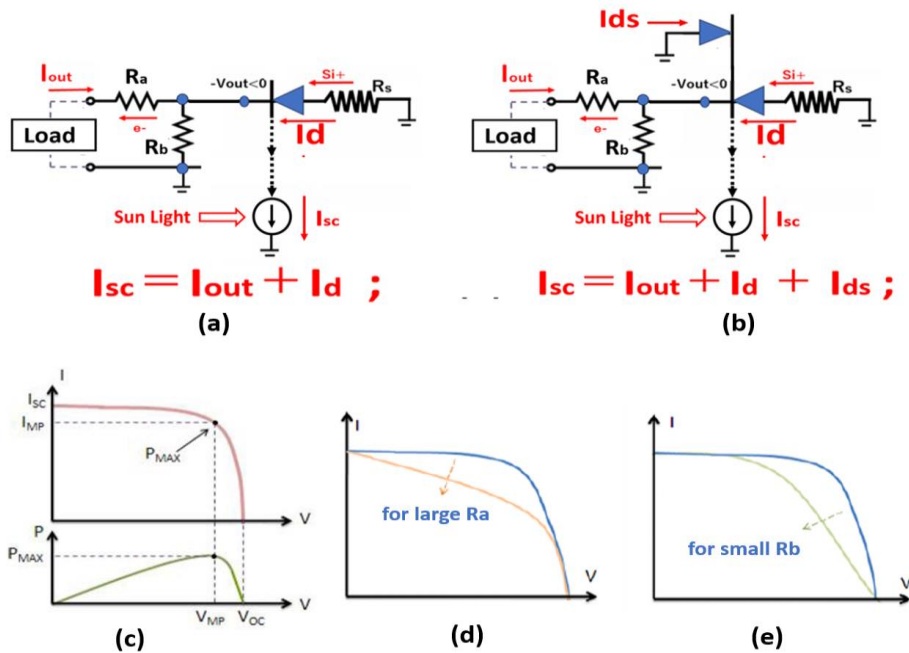


Figure 28. The MPTT scheme applied both for the single and double junction type solar cells.

By changing the values of the resistance R_a and R_b according to the intensity of the sun light, we can adjust the output current I_{out} and optimize the values of the output voltage V_{out} and the output resistance R_{out} for maximum power output [56–57]. In Figure 28a, the photo current $\{I_{sc} = I_{out} + I_d\}$ is the sum of the small-area output current I_{out} and the large-area forward photodiode currents I_d . In Figure 28b, the internal photo current I_{sc} is given as $\{I_{sc} = I_{out} + I_d + I_{ds}\}$ for the double junction photodiode shown, which is the sum of the output current I_{out} and the two forward-biased currents, one as the I_d current for a small-area photodiode and the other one as the I_{ds} current for a large-area photodiode.

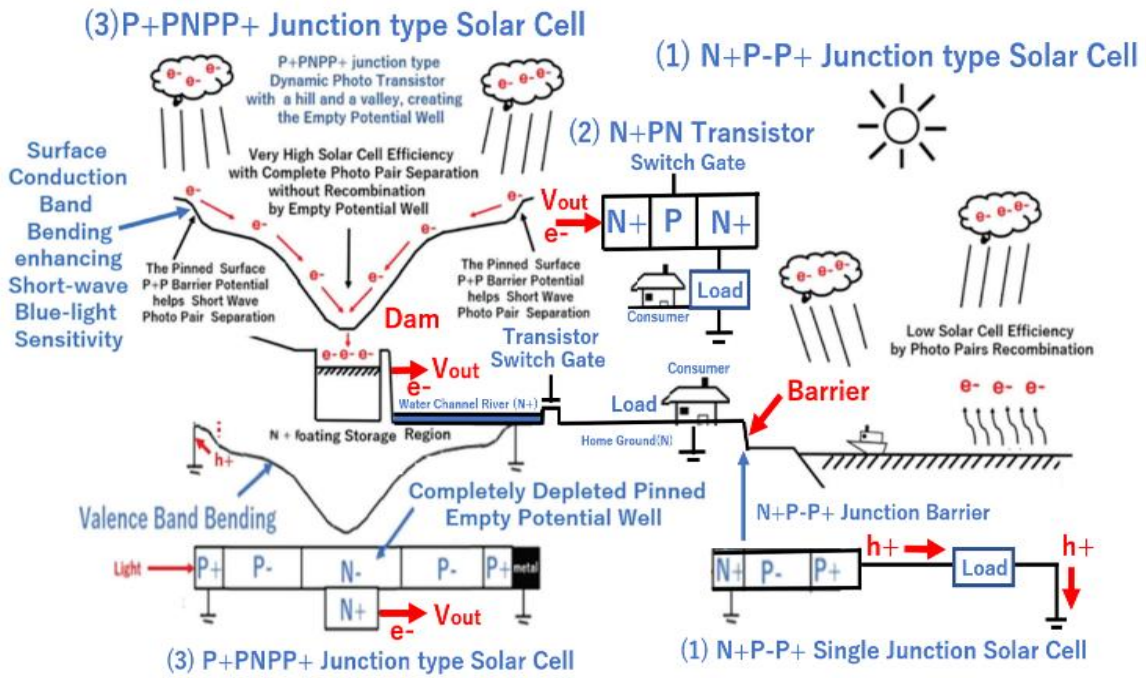


Figure 29. Water Barrier, Water Gate and Water Dam Analogy of Semiconductor Devices [67].

12. Artificial Intelligent Partner System (AIPS) supported by high-performance image sensors

Figure 29 shows an analogy of behaviors of water molecules directed and collected in an underground small-area water storage beneath the large-area, dry and always-empty water-dam. The photo electron charge carriers (electron and hole pairs) behave similarly in the pinned-surface P+PNPP+ double junction photodiode type solar cell structure. The beach wave-front barrier model for a diode and the water-gate model for a switching transistor are well known and well accepted. The concept of the artificial intelligent partner system (AIPS) is explained in Figure 30, which used originally in 2008 Sony Play Station III Cell Processors together with a large number of video cameras to realize a real-time fast-action friendly assistant and care system, supported by the wire-less real-time communication network. Many semiconductor device elements are needed.

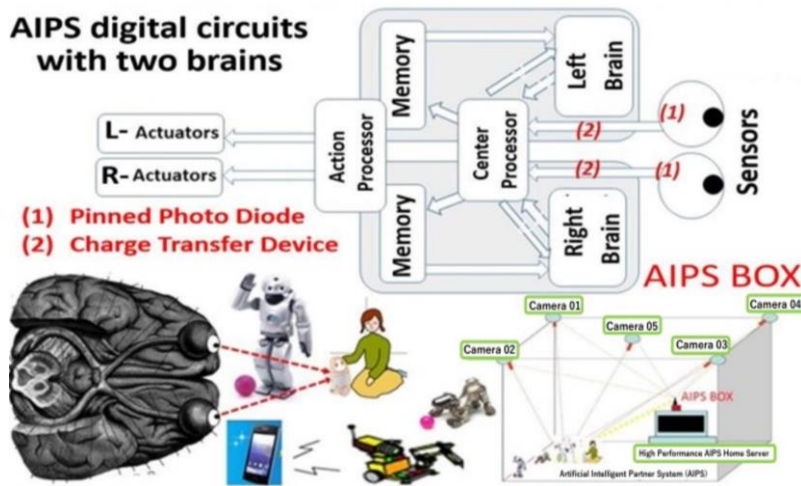


Figure 30. Artificial Intelligent Partner System (AIPS) introduced in 2008 by Sony [68].

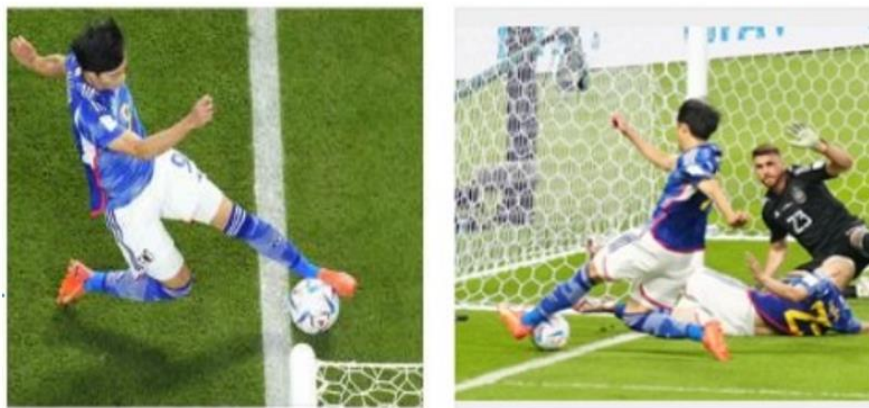


Figure 31. VAR was used in the FIFA at the 2022 World Cup in Qatar [58].

The concept of the video assistant referee (VAR) [59–61], now applied and used worldwide, is very similar to the original concept of the Artificial Intelligent Partner System (AIPS) introduced in 2008.

FIFA's use of VAR at the 2022 World Cup in Qatar was different from the Premier League's use with the addition of a semi-automatic offside system. See Figure 31.

The new element uses 12 dedicated cameras that tracks the ball and all players to calculate their exact position on the pitch. Each camera, installed under the roof of the stadium, receive 50 data points per second. They focus on 29 data points, including every limb of every player and the limbs needed for offside. The match ball will also provide a key element.

The pinned-surface buried-channel photodiode Sony invented in 1975 is now widely known simply as the pinned photodiode (PPD), which a shallow p-type or n-type (respectively) substrate layer, such that the intermediate buried diffusion layer can be fully depleted of majority carriers, such the base region of dynamic bipolar junction transistor [62–63].

The pinned photodiode, usually in the pinned-surface P+PNPP+ double junction type structure, is now used widely in CMOS active-pixel image sensors; a precursor pinned-surface N+NPNP triple junction variant with the MOS buffer capacitor for photo holes as the signal carriers and the back-light illumination scheme with complete charge transfer and no image lag was invented by Sony in 1975. This scheme was widely used in many image sensor applications now.

The artificial intelligent partner system (AIPS) of our future real-time high-performance computing system [64–66] is depending on the massive assemblies of parallel processors over mesh-connected wireless networks to execute vast amounts of computational tasks with vast numbers of sensors of all types in order to assist the way humans and computers interact in order to meet our limit-less human needs. This real-time AI smart vision chip has a sun-light energy-sourced solar cell function capability utilizing a unique high-performance $N \times N$ pixel array of the pinned-surface P+PNPP+ double junction photodiodes with the excellent photon-to-electron conversion efficiency and the highly light-sensitive image-sensor, with a built-in solar cell capability at the same time even at the very low light level, very much more super-sensitive than human eyes [67–69].

13. Summary and Conclusion

The buried-channel type charge coupled device (CCD) is not the only charge transfer device (CTD) that can transfer one single photo electron in the buried-channel N region, which is completely depleted of majority carrier electrons.

The pinned-surface buried-channel P+PNPP+ double junction photodiode can also transfer one single photo electron in the buried-channel N region, which is completely depleted of majority carrier electrons.

The charge transfer gate (CTG) and the pre-charge gate (PCG) are both chosen to be a depletion-type MOS transistor with a negative threshold gate voltage, so that in the external power-off mode, both of the N-type buried-channels under the CTG and the PCG MOS transistors are kept open for photo electrons to flow freely, for passing thru to the outlet drain, which can be switched to the solar cell load.

Classical MOS type CTD image sensors suffered not only the serious image lag problem but also a large undesired CkT thermal noise and high frequency clock noise, degrading the picture quality. Due to these drawbacks, CCD type CTD type image sensors were widely used in image sensor applications, until late 1990s. Thanks to the advancement of CMOS scaled process technology, CCD is now completely replaced by the in-pixel source-follower current-amplifier type charge transfer device.

The double junction solar cell also has also a small-area outlet N+ drain region to connect the solar cell with the external load and the identical external maximum power tracking technology (MPTT) can be applied. Besides, the buried-channel N region, completely depleted of both majority carrier electrons and minority carrier holes, can transport even one single photo electron without recombination in the silicon chip for a long distance, directing photo electrons toward the small-area outlet N+ diffusion region, and very suited for high performance solar cell applications.

A new AI smart robot vision chip in the modern 3DIC CMOS image sensor technology is proposed, which is composed of an array of $N \times N$ pinned-surface buried-channel P+PNPP+ double junction type photo diodes, $N \times N$ analog-data steam mask-and-match comparators, and SRAM cache buffer CMOS memory units. All of them are integrated in a 3-D multichip system with the original 1972 basic architecture designed by Caltech EE graduate students.

In the external power-off mode, as an AI self-energy robot vision chip, the image sensor array of $N \times N$ pinned-surface buried-channel P+PNPP+ double junction type photo diodes can also function as a solar cell energy source unit. By a clever device and circuit design scheme, this array of $N \times N$ pinned-surface buried-channel P+PNPP+ double junction type photo diodes also function as a solar cell unit for the AI self-energy robot vision chip application. This real-time super performance solar cell in the AI smart robot vision chip is in this 3DIC multichip architecture with a unique high-performance unit of the built-in solar-cell and image-sensor combined device structure, which is based on the Sony original 1950s semiconductor process of the P+PNPP+ double junction dynamic bipolar transistor technology with a charge transfer device unit which is based by the modern scaled CMOS 3DIC digital multichip process technology that Sony and many competing companies are developing.

Acknowledgments

First of all, the author would like to express sincere gratitude to Haruo Kobayashi of Gunma University and Toru Sai of Tokyo Polytechnic University for their kind guidance and fruitful discussions and the editorial group for extending kind advice and helps to improve the readability of this technical report.

James McCaldin at California Institute of Technology (Caltech) introduced and taught, in our undergraduate classes, the basic semiconductor device physics at Caltech in 1969 with plenty of side-wall back-ground exciting stories of Intel's unique self-aligned E/D MOS transistor technology and the newly developed high energy ion implantation technology.

C. A. Mead and T. C. McGill at Caltech advised the author the original 1971 undergraduate work on the Ga₂O₃-Au Schottky Barrier interface study and characterization, and also for guiding the Caltech 1974 PhD thesis work on the charge transfer analysis of buried channel CCD image sensors.

The author also expresses sincere gratitude to Motoaki Abe, Yoshiyuki Kawana and Toshio Kato for supporting the original 1978 work at Sony on the first pinned-surface buried-channel P+PNPP+ double junction photodiode that had become the basis for high-performance image sensor applications.

Sony image sensor R/D efforts started in 1969 with the strong initiative of the ex-president of Sony Corporation, Kazuo Iwama, who emphasized the market need of the portable small video camera with the no image lag feature for the real-time fast-action-capturing and snap-shot pictures.

Kazuo Iwama gave the author a chance to work at Sony in 1975 to build an artificial intelligent image sensor system with real-time robot vision and the powerful digital circuit engines for real-time operations.

A long history of SONY bipolar process and device technology gave hints and guidance to the original 1975 inventions and also led to the 1978 successful development of the highly light-sensitive device.

Sony reported the complete charge transfer capability and the no-image-lag feature at the SSDM1978 conference in Tokyo. After a sequence of invited talks at the CCD1975 in Edinburgh Scotland UK in 1979 and at the IEEE ESC1980 conference in St. Louis USA, Sony kept silence and focusing on the efforts in the production and yield enhancement to improve cost-performance. With the understandings and encouragements by Sony president Norio Ohga and the top managements, Sony finally introduced the passport size portable video camera on the market in 1987 after 12 years of pains-taking hard diligent works by many people involved since the 1975 invention.

The author expresses a deep gratitude to the guidance of Sei-ichi Watanabe, and the supporting team of Miyaji and Nakagawara with other young engineers for their successfully developing and reporting at the IEEE ISSCC1989 conference in San Francisco, for the first time in the world, on the 25-nano sec access-time 4 Megabit fast-cache SRAM chip, which was a very essential element to realize a fast-snapshot full-size image capturing system for digital solid-state camera applications. The all-solid-state portable digital camera, which was completely free of any film-media and mechanical parts, opened the gate way to the modern high-definition digital TV and the smart-photon electronic imaging eras.

References

- [1] W. S. Boyle and G. E. Smith, "Charge Coupled Semiconductor Devices", Bell Syst. Tech. J., 49, 1970, pp. 587–593.
- [2] Gordon E. Moore, "Cramming more components onto integrated circuits", Electronics, Volume 38, Number 8, April 19, 1965.
- [3] R. C. Henderson, R. F. W. Pease, A. M. Voshchenkow, P. Mallery, and R. L. Wadsack, "A high speed p-channel random access 1024-bit memory made with electron lithography," in Tech. Dig. Int. Electron Devices Meeting, Dec. 1973, pp.138-140.

- [4] D. L. Spears and H. I. Smith, "X-Ray lithography, a new high resolution replication process," *Solid State Technol.*, vol. 15, p.21, 1972.
- [5] S. Middlehoek, "Projection masking, thin photoresist layers and interference effects," *IBM J. Res. Develop.*, vol. 14, p. 117, 1970.
- [6] R. H. Dennard, F. H. Gaensslen, L. Kuhn, and H. N. Yu, "Design of micron MOS switching devices," presented at the IEEE Int. Electron Devices Meeting, Washington, D.C., Dec. 1972.
- [7] A. N. Broers and R. H. Dennard, "Impact of electron beam technology on silicon device fabrication," *Semiconductor Silicon (ECS Publication)*, H. R. Huff and R. R. Burgess, eds., pp. 830-841, 1973.
- [8] D. L. Critchlow, R. H. Dennard, and S. E. Schuster, "Design characteristics of n-channel insulated-gate field-effect transistors," *IBM J. Res. Develop.*, vol. 17, p. 430, 1973.
- [9] R. H. Dennard et al, "Design of ion-implanted MOSFET's with very small physical dimensions". *IEEE Journal of Solid-State Circuits* **SC-9**, VOL. 87, NO. 4, APRIL 1999.
- [10] P. J. W. Noble, "Self-Scanned Silicon Image Detector Arrays", *IEEE TED*, 15, 1968, pp. 202-209.
- [11] R. H. Walden, et al., "Buried Channel CCD", *Bell Syst. Tech. J.*, 51, 1972, pp. 1635–1640.
- [12] J. Santen et al, JPA1976-65707 and Patent No.7596795 filed on June 9, 1975, Netherland.
- [13] Yoshiaki Daimon Hagiwara, "Chronology of silicon-based image sensor development", *IEEE EDS Newsletter* pp.18-21. Jan 2023. https://eds.ieee.org/images/files/newsletters/Newsletter_Jan23.pdf
- [14] <https://www.sony.com/en/SonyInfo/News/notice/20200626/>
- [15] <https://www.shmj.or.jp/english/pdf/dis/exhibi1005E.pdf>
- [16] Yoshiaki Daimon Hagiwara, and Kikuyo Ishikawa, an invited talk, "AIPS with Pinned Buried Photodiode used for Robot Vision and Solar Cell Panel", *ICCCAS2023*, Singapore, May, 2023 and *IEEE AIPE2023* conference, Tokyo Japan, Oct 2023. <https://ieeexplore.ieee.org/document/10473244>
- [17] H. Yagi, T. Tsuyuki, K. Koma and Y. Miyazawa, "A novel bipolar device with low emitter impurity concentration structure", *IEEE Int. Electron Devices Meeting (IEDM1974)*, Washington DC, USA.
- [18] Kazuo Nishiyama, "Invention of Lamp Anneal", Japanese Patent No. 1386103, JPA1981-32311.
- [19] J. Hynccek, "Virtual phase CCD technology", in *IEEE Proc. IEDM*. Dec. 1979, pp.611-614.
- [20] N. Teranishi, Y. Ishihara and H. Shiraki, Japanese Patent Application JPA1980-138026.
- [21] N. Teranishi, et al., "No image lag photodiode structure in the interline CCD image sensor", *IEEE International Electron Devices Meeting*, Dec 1982, pp. 324-32
- [22] B. C. Burkey et al. "The Pinned Photodiode for an Interline-transfer CCD Image Sensor", *Int. Electron Devices Meeting*, 1984, pp. 28-31.
- [23] S. Sreejith, J. Ajayan, Sreedhar Kollem & B. Sivasankari, "A Comprehensive Review on Thin Film Amorphous Silicon Solar Cells", January 2022, Volume 14, pages 8277-8293, Springer Link (2022),
- [24] C.A. Mead et al, "128-Bit Multi Comparator", *Caltech/Intel Project 1972-1973*, *IEEE Journal of Solid-State Circuits*, VOL.SC11, No.4, Oct.1976.
- [25] M. Sakakibara, et al, "A Back-illuminated Global-Shutter CMOS Image Sensor with Pixel-Parallel 14b Subthreshold ADC", *ISSCC2018*, Feb. 2018
- [26] Y. Kumagai, et al, "Back-illuminated 2.74 um-Pixel-Pitch Global Shutter CMOS Image Sensor with Charge-Domain Memory Achieving 10k e- Saturation Signal " *IEDM2018*, Dec 2018.
- [27] Y. Kagawa and H. Iwamoto, "3D Integration Technologies for Stacked CMOS Image Sensors", an invited paper at the *IEEE 3DIC2019* conference, Oct 8, 2019, Sendai, Japan.

- [28] Fumio Miyaji et al "A 25 nano sec 4 Mega bit CMOSRAM with Dynamic Bot-Line Loads", the ISSCC1989 conference Feb. 1989 and J. Solid State Circuits, Vol. 24, No. 5, October 1989.
- [29] M. Hamasaki, et al., "An IT-CCD image with electronically variable shutter speed", Tech. Rep. Institute of Image Information and Television Engineers in Japan. vol. 12, no. 12, pp. 31-36., 1988.
- [30] K. Ishikawa et al. at Sony, "IT CCD Imaging Sensor with Variable Speed Electronic Shutter", IEEE Proc. SPIE 1107, October 1989.
- [31] Ryoji Suzuki, Keiji Mabuchi, Tomonori Mori, Japanese Patent Number 3759435.
- [32] M. Sakakibara, et al, "A Back-illuminated Global-Shutter CMOS Image Sensor with Pixel-Parallel 14b Subthreshold ADC", ISSCC2018, Feb. 2018
- [33] Y. Kumagai, et al, "Back-illuminated 2.74 um-Pixel-Pitch Global Shutter CMOS Image Sensor with Charge-Domain Memory Achieving 10k e- Saturation Signal " IEDM2018, Dec 2018.
- [34] Y. Kagawa and H. Iwamoto, "3D Integration Technologies for Stacked CMOS Image Sensors", an invited paper at the IEEE 3DIC2019 conference, Oct 8, 2019, Sendai, Japan
- [35] Taku Umebayashi, Hiroshi Takahashi, Japanese Patent Number 5773379.
- [36] Jun-ichi Nishizawa, <https://www.shmj.or.jp/english/pioneers/pnr13.html>
- [37] M. Sun, K. Xie, Y. Lu, "Robust PIN photodiode with a guard ring protection structure", IEEE Trans. Electron. Dev. **51**(6), 833–838 (2004). <https://doi.org/10.1109/ted.2004.827374>
- [38] C. Okada et al, "An Interline Transfer CCD Imager with High Density Structure", in Tech. Papers, Institute of Electronics and Communication Engineers of Japan, No. SSD78-5, pp.31-40, April 1978.
- [39] S. Komuro et al, "A System of Three-chip CCD Color Camera", in Tech. Papers, Institute of Television Engineers of Japan, No. TBS46-3, pp. 13-17, May 1978.
- [40] H. Matsumoto, et al "Zigzag transfer CCD image sensor", Professional Group on Semiconductor, Semiconductor Device Institute of Electron. Communication Engineer, Japan, vol.SSD-77, no.3, 1977.
- [41] S. Yamanaka et al, "A color camera employing zigzag-transfer CCDs with checker-pattern" in Tech. Papers, Symp. TBS36, Inst. of Television Engineers of Japan, No. TBS36-3, pp.1-18, Feb. 1977.
- [42] T. Shimada et al, "Frame transfer CCD image sensor with SiO₂ exposed sensor array", in Prof. Gp Semiconductor. Semiconductor Device of Inst. Electron. Com. Eng. Japan, vol.SSD-77, no.2, 1977.
- [43] M. Shimada et al, "A CCD color camera employing exposed sensors and unique sampling technique" in Tech. Papers, Symp. TBS36, Inst. of Tel. Eng. of Jp, No. TBS36-2, pp.1-19, Feb. 1977.
- [44] Andy S, Grove, "Physics and Technology of Semiconductor Devices", John Wiley & Sons, Inc., 1967, Library of Congress Card Number: 67-17340.
- [45] Faggin and T. Klein, "Silicon gate technology," Solid-State Electron., vol 13, pp. 1125-114, 1970.
- [46] Ben G, Streetman, "Solid State Electronic Devices", Prentice Hall, 1972, ISBN 0-13-158767-6.
- [47] Y. Cheng and L. Ding, "Perovskite/Si tandem solar cells: Fundamentals, advances, challenges, and novel applications", Wiley On-line Library, SusMat, Vol. 1, Issue 3, Sept 2021.
- [48] M. Killi and S. Samanta, "Voltage-sensor-based MPPT for stand-alone PV systems through voltage reference control", IEEE J. Emerg. Sel. Top. Power Electron. 2018, 7, 1399–1407.
- [49] L. Musong et al, "A Comprehensive Review of Maximum Power Point Tracking (MPPT) Techniques Used in Solar PV Systems", Energies 2023, 16(5), 2206; Feb 2023.
- [50] Max Jammer, "The conceptual development of quantum mechanics.", McGraw-Hill. p. 51. ISBN0-88318-617-9.

- [51] O. Passon and J. Grebe-Ellis, "Planck's radiation law, the light quantum, and the prehistory of indistinguishability in quantum mechanics". *European J. of Physics*. 38 (3), ISSN 0143-0807.
- [52] Tomokazu Kogure and Kam-Ching Leung, "Thermodynamic equilibrium and blackbody radiation". *The astrophysics of emission-line stars*. Springer. p. 41. ISBN 978-0-387-34500-0.
- [53] Sun Light Power Spectrum is now widely available. See <https://en.wikipedia.org/wiki/Sunlight>
- [54] William Shockley and Hans Queisse, "Detailed Balance Limit of Efficiency of Single PN junction Diode", *Journal of Applied Physics*, Vol 32, pp.510-519,1961.
- [55] Takashi Kita, "Energy Conversion Efficiency of Solar Cell", pp. 113-114, Corona Publisher, Oct 2012, ISBN978-4-339-00842-5.
- [56] Takanori Matsuyama et al, "Experimental Introduction of Distributed Maximum Power Point Tracking Systems for PV System and Effect Applied to Solar Car", *Solar Energy*, Vol. 33, No.4.
- [57] Yosuke Tomita, Yoshiyuki Nagai, Takumi Arai, Masanori Saito, Tsutomu Tanimoto and Kumihiro Nishijima, "MPPT operation performance of automotive photovoltaic system during driving", *IEEE Journal of Industry Applications*, J=STAGE DOI:10.1541/ieejia.22007903, April, 2023.
- [58] FIFA's controversial VAR system, <https://www.wired.com/story/var-football-world-cup/>
- [59] R. A. Hamzah and S. I. Md Salim, "Software Calibration for Stereo Camera on Stereo Vision Mobile Robot using Tsai's Method," *Int. J. of Computer Theory and Eng.* vol. 2, no. 3, pp. 390-394, 2010.
- [60] M. A. de Lemos, E. V. Liberado, A. Galdenoro, "Machine Vision and Planning applied on Assembly Line of Multiple Products," *Int. J of Computer Theory and Engineering* vol. 4, no. 3, pp. 422-425, 2012.
- [61] M. F. Zakaria, H. S. Choon, and S. I A. Suandi, "Object Shape Recognition in Image for Machine Vision Application," *Int. J. of Computer Theory and Engineering* vol. 4, no. 1, pp. 76-80, 2012.
- [62] Michael Riordan and Lillian Hoddeson, "The Invention of the Transistor and the Birth of the information Age", ISBN9780393318517, W. W. Norton & Company, 1998.
- [63] "The Phototransistor", *Bell Lab Record*, May 1950. <https://we.archive.org/web/20150704010847>.
- [64] "MOS Integrated Circuits" by W. M. Penny and L. Lau, New York: Van Nostrand Reinhold, 1972.
- [65] R. W. Keyes, "Physical Limits in Digital Electronics", *IEEE Proceedings*, vol. 63, no. 5, May 1975.
- [66] C. A. Mead and Lynn Conway, "Introduction to VLSI systems", Addison-Wesley Series in Computer Science, 1980, ISBN 0-201-04358-0, Addison-Wesley Publishing Company.
- [67] Yoshiaki Hagiwara, "The World of Digital Circuits for Artificial Intelligent Partner System (AIPS)", ISBN978-4-88359-339-2, 450 pages, Hard Cover, Seizan-sha Publishing, 2016.
- [68] Yoshiaki Hagiwara, Japanese Patent No. 6818208, JPA 2020-131313 filed on August 1, 2020.
- [69] Yoshiaki Daimon Hagiwara, "Dynamic Photo Transistors for Image Sensors and Solar Cells", Key Note Speech at the ICDIS2024 conference, Xiamen, China, Nov 22-23, 2024.
- [70] Yoshiaki Daimon Hagiwara, Caltech PhD Thesis, June 1975, more details: <http://www.aiplab.com>